

Chaotic Variability of the Atlantic Meridional Overturning Circulation at Subannual Time Scales

AGATHE GERME,^a JOËL J.-M. HIRSCHI,^a ADAM T. BLAKER,^a AND BABLU SINHA^a

^a *National Oceanography Centre, Southampton, United Kingdom*

(Manuscript received 7 May 2021, in final form 18 November 2021)

ABSTRACT: This study describes the intra- to interannual variability of the Atlantic meridional overturning circulation (AMOC) and the relative dynamical contributions to the total variability in an eddy-resolving 1/12° resolution ocean model. Based on a 53-yr-long hindcast and two 4-yr-long ensembles, we assess the total AMOC variability as well as the variability arising from small differences in the ocean initial state that rapidly imprints on the mesoscale eddy fields and subsequently on large-scale features. This initial-condition-dependent variability will henceforth be referred to as “chaotic” variability. We find that intra-annual AMOC fluctuations are mainly driven by the atmospheric forcing, with the chaotic variability fraction never exceeding 26% of the total variance in the whole meridional Atlantic domain. To understand the nature of the chaotic variability we decompose the AMOC (into its Ekman, geostrophic, barotropic, and residual components). The barotropic and geostrophic AMOC contributions exhibit strong, partly compensating fluctuations, which are linked to chaotic spatial variations of currents over topography. In the North Atlantic, the largest chaotic divergence of ensemble members is found around 24°, 38°, and 64°N. At 26.5°N, where the AMOC is monitored by the RAPID–MOCHA array, the chaotic fraction of the AMOC variability is 10%. This fraction is slightly overestimated with the reconstruction methodology as used in the observations (~15%). This higher fraction of chaotic variability is due to the barotropic contribution not being completely captured by the monitoring system. We look at the strong AMOC decline observed in 2009/10 and find that the ensemble spread (our measure for chaotic variability) was not particularly large during this event.

SIGNIFICANCE STATEMENT: The ocean is characterized by ubiquitous swirls (eddies) with diameters ranging from more than 100 km (low latitudes) to a few tens of kilometers (high latitudes). There is limited predictability of the timing and location of such eddies. They introduce unpredictable (“chaotic”) variability, which affects the ocean circulation on a wide range of spatial and temporal scales. Any observations of ocean currents contain a fraction of chaotic variability. However, it is, in general, not possible to quantify this chaotic variability from observations. Here we use a set of simulations performed with a state-of-the-art ocean computer model to estimate the fraction of chaotic variability in the amount of warm northward flowing near-surface seawater that delivers large amounts of heat to the North Atlantic, known to scientists as the Atlantic meridional overturning circulation (AMOC). We find that about 10%–25% of the AMOC variance is likely to be chaotic.


KEYWORDS: Ocean; Eddies; Meridional overturning circulation; Mesoscale processes; Ocean models

1. Introduction

The Atlantic meridional overturning circulation (AMOC) is an important feature of the large-scale ocean circulation [see [Buckley and Marshall \(2016\)](#) for a review]. It redistributes heat globally and influences the climate of the surrounding regions (e.g., [Knight et al. 2005](#); [Latif et al. 2006](#); [Gastineau and Frankignoul 2012](#)). According to modeling studies, it has strong decadal to multidecadal variability although this has not been observed yet due to the lack of sufficiently long observed time series. Since April 2004 the RAPID–MOCHA array with its continuous twice-daily measurements of the AMOC revealed a large subannual variability of the AMOC ([Cunningham et al. 2007](#); [Chidichimo et al. 2010](#); [Kanzow et al.](#)

[2010](#); [Duchez et al. 2014](#); [Smeed et al. 2018](#)), deeply changing its perceived picture. There is also emerging evidence that the AMOC may impact on the North Atlantic heat content ([Sonnewald et al. 2013](#); [Bryden et al. 2014](#)) and sea surface temperature ([Duchez et al. 2016a](#)) at these time scales. Although the impact of this subannual variability might be sensitive to the period considered ([Alexander-Turner et al. 2018](#)), it could be important for the prediction of seasonal climate events (e.g., [Buchan et al. 2014](#); [Duchez et al. 2016b](#); [Hallam et al. 2019](#)).

For a dynamical system, chaotic behavior can be defined as a strong sensitivity to initial conditions, i.e., slightly different initial conditions can evolve into considerably different states ([Lorenz 1963](#)). In the climate system, the atmosphere is very well known to exhibit such behavior, thereby limiting the

 Denotes content that is immediately available upon publication as open access.

Corresponding author: Joël Hirschi, joel.hirschi@noc.ac.uk



This article is licensed under a [Creative Commons Attribution 4.0 license](http://creativecommons.org/licenses/by/4.0/) (<http://creativecommons.org/licenses/by/4.0/>).

DOI: 10.1175/JPO-D-21-0100.1

© 2022 American Meteorological Society.

skillful prediction of weather patterns to a couple of weeks (Lorenz 1982). Ocean mesoscale eddies are the equivalent of weather systems in the atmosphere. As their atmospheric counterparts the timing, location of the formation of ocean eddies cannot be predicted and the prediction of their evolution is limited to week to perhaps months. Mesoscale eddies are thought to have a major impact on the mean ocean circulation (e.g., Rhines 1977; Salmon 1980; Hochet et al. 2020; Sévellec et al. 2021). However, how and on what time scales they can affect the variability of the large-scale ocean circulation is far from fully understood.

Numerical ocean model simulations forced by a repeated atmospheric annual cycle, have shown that ocean chaotic variability emerges spontaneously when mesoscale eddies are permitted by the model resolution (Thomas and Zhai 2013; Grégorio et al. 2015). At interannual-to-decadal time scales, this chaotic variability has been found to account for one-third to one-half of the total variance of the AMOC around 25°N, while it accounts for only 5%–10% of the total variance in the subpolar region. Using a different approach based on a large ensemble of eddy-permitting ocean hindcasts sharing the same atmospheric forcing but with slightly different initial conditions, Leroux et al. (2018) found similar results, showing that the amount, meridional distribution, and space–time spectral characteristics of chaotic variability under realistic atmospheric forcing are in good agreement with those of Grégorio et al. (2015). These estimates, focusing mainly on interannual to decadal time scales, might not reflect the fraction of AMOC variability arising from oceanic processes at shorter time scales. Using a pair of twin eddy permitting experiments, Hirschi et al. (2013) estimated the chaotic contribution of the total sub to interannual AMOC variance to be approximately 9%, implying that the atmosphere plays a dominant role in driving short-term AMOC variability. In accordance with these findings, Roberts et al. (2013) found that the atmosphere played a dominant role in the short-term decline of the AMOC observed in 2009/10 (McCarthy et al. 2012; Bryden et al. 2014).

At 26.5°N, the RAPID–MOCHA array measurements (Cunningham et al. 2007; Smeed et al. 2018) could be sensitive to this chaotic variability. Indeed, the RAPID AMOC time series is based on the sum of three components: the Ekman, the Florida Strait, and the upper midocean transport. The latter is retrieved through the thermal wind relation using observations taken by a set of moorings at the boundaries. The western boundary is a region of significant eddy activity, and the effect of eddies and waves propagating westward from the basin interior on the geostrophic transport at subannual time scale could be substantial (de Verdière and Tailleux 2005). For example, random eddies were suspected to dominate the AMOC fluctuations up to 16 Sv ($1 \text{ Sv} \equiv 10^6 \text{ m}^3 \text{ s}^{-1}$) at this time scale (Wunsch 2008). However, taking into account their energy decrease at the proximity of the boundary showed that the variability attributable to eddies and waves would be of the order 4 Sv (Kanzow et al. 2009), or even 2.6 Sv when taking into account the vertical structure of the eddies (Clément et al. 2014).

In this analysis, we use an eddy-resolving $1/12^\circ$ resolution ocean model to characterize the full meridional structure of the AMOC variability at sub- to interannual time scales and the relative contributions of different dynamical processes to this variability. Following the approach of Leroux et al. (2018), the chaotic variability of the AMOC and its components is assessed. Finally, implications for the monitoring of the AMOC by the RAPID–MOCHA array at 26.5°N are discussed.

2. Data and methodology

In the following we describe the numerical ocean model and simulations used in this study (section 2a) as well as the RAPID observations from 26.5°N (section 2b). We also introduce three complementary approaches to compute the AMOC in the model (section 2c). We note that the use of three approaches may initially appear excessive, but the reason will become clear later in the paper when we try to understand the origin of the chaotic AMOC variability we find in the model.

a. Model and simulations

We use the NEMO v3.6 ocean model (Madec et al. 2016) in the ORCA12 configuration corresponding to a nominal resolution of $1/12^\circ$ (Marzocchi et al. 2015). At 26.5°N the resolution is approximately 8.3 km. There are 75 vertical levels ranging from 1 m at the surface to 250 m at the bottom. Bottom topography is represented as partial steps and bathymetry is derived from ETOPO2 (NOAA 2006). The model includes the sea ice model LIM2 (Louvain-la-Neuve Sea Ice Model; Fichefet and Maqueda 1997; Timmermann et al. 2005).

Based on this model configuration we use a 53-yr-long ocean hindcast already used for North Atlantic variability studies (Moat et al. 2016) and henceforth referred to as N006. It starts from rest with climatological initial conditions for temperature and salinity from the Polar Science Center Hydrographic Climatology PHC2.1 (Steele et al. 2001) at high latitudes, MEDATLAS (Jourdan et al. 1998) in the Mediterranean, and Levitus et al. (1998) elsewhere. It simulates the 1958–2012 period using the Drakkar Surface Forcing dataset version 5.2 (Dussin et al. 2014; Brodeau et al. 2010), which supplies surface air temperature, winds, humidity, surface radiative heat fluxes, and precipitation. To prevent excessive drifts in global salinity due to deficiencies in the freshwater forcing, sea surface salinity is relaxed toward climatology with a piston velocity of $-33.33 \text{ mm day}^{-1} \text{ psu}^{-1}$. Model output is stored as 5-day averages. We restrict our analysis to the period 1960–2012 to allow the eddy field sufficient time to develop.

Starting from this integration, two 3-member initial condition perturbation ensembles have been performed starting from 1 January 2007 and 2009, respectively. The initial condition perturbations are generated by lagging the oceanic initial conditions by 1–3 time steps from the N006 run and all members are integrated for 4 years using the same model configuration and surface forcing. We note that since we use a forced

ocean model for our experiments we can only estimate the chaotic AMOC variability in the situation where the ocean cannot influence the atmospheric circulation. This of course is not the case in a coupled system where the chaotic variability of both ocean and atmosphere would project onto the AMOC and lead to a larger divergence between ensemble members than in the experiments we discuss here.

b. The AMOC observation dataset

We use the observation-derived transport estimates from the RAPID array at 26.5°N. In this estimate, the AMOC is constructed as the sum of three components: an estimate of the Florida Strait transport is obtained from the electrical voltage induced in a submerged telephone cable that lies between mainland Florida and the Bahamas (Meinen et al. 2010), the Ekman transport calculated from the ERA-Interim wind field (Dee et al. 2011), and the upper midocean transport assessed from a set of moorings across 26.5°N from the Bahamas to the African coast (Rayner et al. 2011). Since April 2004 the array has provided twice daily transport estimates based on these observations, revealing an unprecedented picture of the AMOC variability at subannual to multiannual time scales at this latitude (Srokosz and Bryden 2015). For comparison with the model simulations, we produce 5-day averages from the RAPID–MOCHA observations in accordance with the 5-day mean output of the model.

c. AMOC decompositions

A dynamical decomposition of the simulated AMOC helps to highlight dominant mechanisms accounting for the AMOC fluctuations. In this section, three different decompositions of the AMOC are detailed. The first one corresponds to the decomposition introduced by Lee and Marotzke (1998), considering the AMOC as the sum of the transport arising from surface wind forcing (Ekman), an external mode with variable topography, the vertical shear due to thermal wind balance, and a residual ageostrophic contribution. This decomposition can be used at any latitude in the Atlantic domain. The second decomposition corresponds more closely to the component parts of the observing system used for the RAPID–MOCHA array measurements, and therefore rely on measurement feasibility at 26.5°N. Finally, the third decomposition is based on the RAPID–MOCHA array decomposition, with a specific change in order to investigate the role of the external mode partly captured in the upper midocean contribution on the reconstructed AMOC variability at 26.5°N. The equations in section 2c(1) are applied for all latitudes in the Atlantic, while the 26.5°N specific treatment of Florida Straits given in sections 2c(2) and 2c(3) are only computed at this latitude.

1) FULL AMOC DECOMPOSITION: ψ_{full}

The AMOC, ψ_{full} , is defined as the zonal and vertical integral of the meridional velocity:

$$\psi_{full}(z) = \int_{-H_{max}}^z \int_{x_w}^{x_e} v(z') dx dz', \quad (1)$$

where v corresponds to the meridional velocity; H_{max} corresponds to the maximum depth of the basin at 26°N; z is the vertical coordinate; and x_w and x_e are the western and eastern boundaries of the ocean basin, respectively.

We decompose the AMOC into one barotropic and three baroclinic components as follows:

$$\psi_{full} = \psi_{BTR} + \psi_{GEOSH} + \psi_{EKM} + \psi_{RES}, \quad (2)$$

where ψ_{BTR} corresponds to the barotropic component, i.e., the zonal and vertical integral of the barotropic meridional velocity \bar{v} :

$$\psi_{BTR}(z) = \int_{-H_{max}}^z \int_{x_w}^{x_e} \bar{v}(x) dx dz' \quad (3)$$

with

$$\bar{v}(x) = \frac{1}{H(x)} \int_{-H(x)}^0 v(x, z') dz'. \quad (4)$$

This component has been referred to as the external mode (e.g., Lee and Marotzke 1998; Sime et al. 2006; Hirschi and Marotzke 2007). Other definitions of the external mode have been used in other studies [e.g., Buckley and Marshall (2016), who rather use the section-wide section average velocity rather than the velocity \bar{v} according to Eq. (4)]. All definitions have in common that the external mode only projects onto the AMOC when flow occurs over sloping topography. The definition of the external mode as in Eqs. (3) and (4) is also in keeping with what we know from observations about the nature of the flow along the western boundary (at least close to 26.5°N). Indeed Bryden et al. (2009) show that transport fluctuations through the Florida Straits are compensated by a barotropic flow just east of Bahamas. To represent this situation the external mode using our approach seems to be a reasonable choice: the Florida current contains a large barotropic contribution and due to the approximately step-wise bathymetry at the western boundary this results in a vigorous external mode of 25–30 Sv which is well captured by Eqs. (3) and (4).

As there is currently no strategy to monitor the barotropic velocity, this mode cannot be directly retrieved from the RAPID–MOCHA array measurement.

The term ψ_{EKM} is the Ekman component compensated by a section mean return flow to ensure no net transport:

$$\psi_{EKM}(z) = \int_{-H_{max}}^z \int_{x_w}^{x_e} [v_{EKM}(z) - \bar{v}_{EKM}] dx dz', \quad (5)$$

where v_{EKM} and \bar{v}_{EKM} are

$$v_{EKM} = \frac{1}{(\rho^* f L \Delta_z)} \int_{x_w}^{x_e} \tau_x dx, \text{ and} \quad (6)$$

$$\bar{v}_{EKM} = -\frac{1}{(\rho^* f A)} \int_{x_w}^{x_e} \tau_x dx, \quad (7)$$

where $L = x_e - x_w$ is the basin width at the surface, ρ^* a reference density, Δ_z the Ekman layer depth, and H_{max} the maximum depth of the longitude–depth section.

This component can be fully derived from the zonal wind stress accessible through satellite and ship measurements. The Ekman layer depth, Δz , which defines the base of the Ekman layer in which the wind driven transport occurs, is chosen to be 100 m. Under this layer, v_{Ekm} is assumed to be zero.

The term $\psi_{\text{GEO SH}}$ is the geostrophic shear component arising from the zonal density gradient across the Atlantic basin:

$$\psi_{\text{GEO SH}}(z) = \int_{-H_{\text{max}}}^z \int_{x_w}^{x_e} [v_{\text{GEO}}(x, z') - \overline{v_{\text{GEO}}}(x)] dx dz', \quad (8)$$

where the geostrophic velocity arises from the thermal wind balance as

$$v_{\text{GEO}}(x, z) = \frac{-g}{\rho^* f} \int_{-H(x)}^z \frac{\partial \rho}{\partial x} dz', \quad (9)$$

with g the gravitational acceleration, f the Coriolis parameter, ρ the local density, and $\overline{v_{\text{GEO}}}$ is the depth averaged geostrophic velocity:

$$\overline{v_{\text{GEO}}}(x) = \frac{1}{H(x)} \int_{-H(x)}^0 v_{\text{GEO}}(x, z') dz'. \quad (10)$$

Finally, ψ_{RES} is the baroclinic ageostrophic residual obtained by rearranging Eq. (2),

$$\psi_{\text{RES}} = \psi - (\psi_{\text{BTR}} + \psi_{\text{GEO}} + \psi_{\text{EKM}}). \quad (11)$$

Note that, unlike for other decompositions, the Gulf of Mexico has been taken into account in this decomposition in order to allow for a possible projection of the Gulf Stream (via the Loop Current) on the AMOC. This also means that the flow at 26.5°N is not fully consistent with other decompositions.

2) RAPID-LIKE RECONSTRUCTION: ψ_R

The AMOC reconstruction of the RAPID array at 26.5°N is based on the decomposition introduced in the previous section, but adapted in order to use quantities that can be measured in the real ocean as described in [Hirschi and Marotzke \(2007\)](#). It aims at monitoring the AMOC between Florida and the African coast and therefore excludes the Gulf of Mexico, hereby considering a different domain from the decomposition of ψ_{full} at this latitude.

First, the transport through the Florida Straits is directly computed as the integration of the meridional velocity in the model:

$$\psi_{\text{FS}} = \int_{-H_{\text{FS}}}^0 \int_{x_F}^{x_B} v(x, z') dz' dx \quad (12)$$

where x_F , x_B denote the western (Florida) and eastern (Bahamas) margins of the Florida Straits.

In the main basin, the difficulty arising from the previous decomposition in the RAPID-MOCHA array is the inability of current observational techniques to assess the barotropic velocity \bar{v} [Eq. (4)] preventing the direct measurement of the external mode [Eq. (2)]. However, as shown in [Hirschi and Marotzke \(2007\)](#), under the assumption of the bottom velocity

being zero, the geostrophic velocity v_{GEO} contains both baroclinic and barotropic [referred as $\overline{v_{\text{GEO}}}$ in Eq. (10)] components, the latter containing valuable information to assess the external mode. In this RAPID-like decomposition, we compute the streamfunction arising from the density at the boundaries, following the assumption of zero bottom velocity. A compensation velocity is introduced to fulfil the mass conservation. This streamfunction therefore contains the geostrophic shear component as well as part of the barotropic component and can be written as

$$\psi_{\text{UMO}}(z) = \int_{-H_{\text{max}}}^z \int_{x_w}^{x_e} [v_{\text{GEO}}(x, z') - \tilde{v}_{\text{comp}}] dx dz' \quad (13)$$

with

$$\tilde{v}_{\text{comp}} = \frac{1}{A} \int_{-H_{\text{max}}}^z \int_{x_B}^{x_e} [v_{\text{GEO}}(x, z')] dx dz' + \frac{\psi_{\text{FS}}}{A}, \quad (14)$$

which corresponds to the transport imbalance across a longitude–depth section divided by the section area

$A = \int_{H_{\text{max}}}^0 dz \int_{x_e}^{x_w} dx$. This contribution, ψ_{UMO} , is referred to as the upper midocean contribution (UMO) as is done in the observations. We note here that using the compensation \tilde{v}_{comp} means that we neglect the meridional transport (i.e., the Bering Strait) transport as its effect on the inferred AMOC variability is negligible.

Finally, the Ekman component is assessed through the main basin following Eq. (5), where the western boundary is taken as x_B . The total AMOC is then reconstructed by summing these three components as

$$\psi_R(z) = \psi_{\text{FS}} + \psi_{\text{UMO}} + \psi_{\text{EKM}}. \quad (15)$$

3) THE RAPID-LIKE GEOSHEAR RECONSTRUCTION:

ψ_{R-B}

To isolate and test the impact of the barotropic component included in ψ_{UMO} , we use a third decomposition very similar to the RAPID-like decomposition introduced in [section 2c\(2\)](#), but remove the depth averaged geostrophic velocity as done in Eq. (8). In this last decomposition, the term ψ_{UMO} in Eq. (15) is then replaced by

$$\psi_{\text{UMO}}(z) = \int_{-H_{\text{max}}}^z \int_{x_B}^{x_e} [v_{\text{GEO}}(x, z') - \overline{v_{\text{GEO}}}(x)] - \frac{\psi_{\text{FS}}}{A} dx dz', \quad (16)$$

similar to Eq. (8), but with x_B taken as the western boundary. Compared to ψ_R , the barotropic part of the information included in the UMO component is lost.

3. Characterization of the AMOC variability and of its components

a. Total variability

The AMOC mean and variability in the ORCA12 configuration are shown in [Figs. 1a](#) and [2a](#), respectively, over the

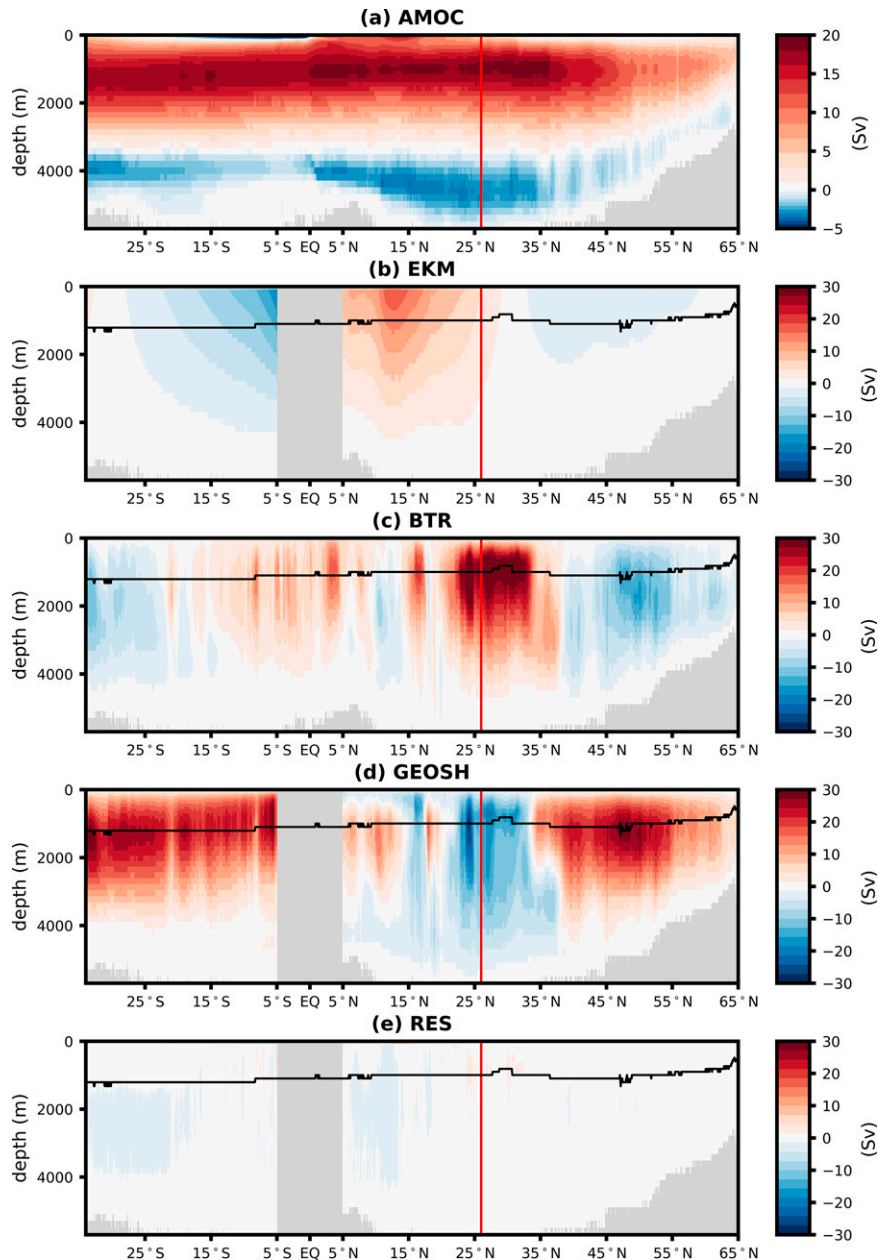


FIG. 1. Time mean of (a) AMOC, (b) Ekman, (c) barotropic, (d) geostrophic, and (e) residual streamfunctions in the N006 simulation. The time average is done over the 1960–2012 period. The solid black line corresponds to the depth of the AMOC index, i.e., the depth of the maximum value of the AMOC streamfunction within 500–2000 m. The vertical red line indicates 26.5°N, i.e., the RAPID–MOCHA array position.

1960–2012 period. The upper AMOC cell ranges from the surface to roughly 3500 m depth, with a maximum transport of about 19 Sv around 35°N. Based on 5-day averages over a 52-yr-long period, the variability is strongly dependent on the latitude. Its highest amplitude is found around the equator where a standard deviation of 21 Sv is reached. Apart from the equator, the largest variability is found around 35°N where it reaches about 5 Sv. This main structure does not

depend strongly on the model resolution, as it is very similar to the variability found with 1/4° resolution (e.g., [Blaker et al. 2012](#); [Hirschi et al. 2013](#)).

As explained in [Jayne and Marotzke \(2001\)](#), a strong variability around the equator is expected from the wind-driven fluctuations of the Ekman transport, compensated by a depth-independent return flow on the whole water column, which explains the vertical extension of the variability maximum.

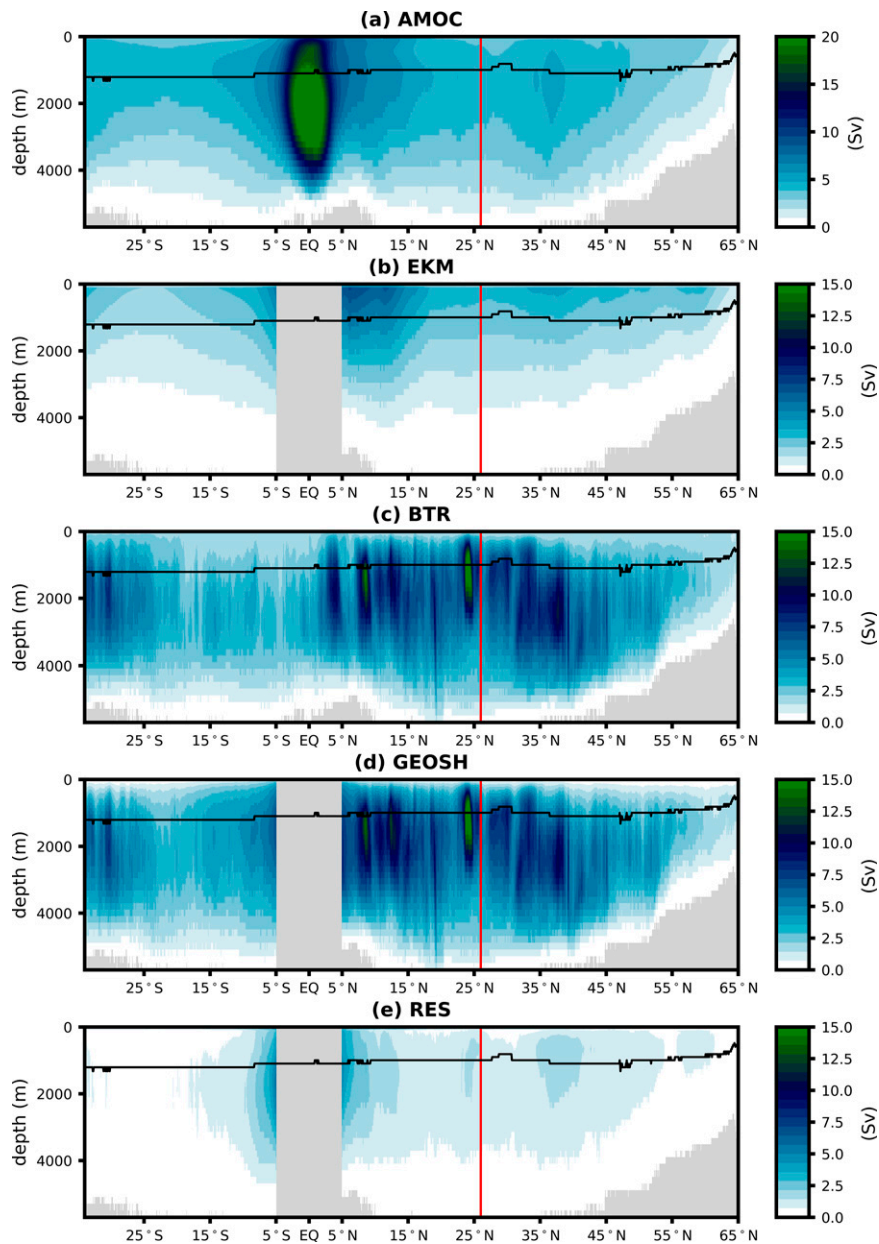


FIG. 2. Time standard deviation of (a) the AMOC, (b) Ekman, (c) barotropic, (d) geostrophic, and (e) residual streamfunctions. Time standard deviation is computed from 5-day mean outputs over the 1960–2012 period. The solid black line corresponds to the depth of the AMOC index, i.e., the depth of the maximum value of the time-mean AMOC streamfunction within 500–2000 m. The vertical red line indicates 26.5°N, i.e., the RAPID–MOCHA array position.

However, model simulations yield variability that is much higher than expected from Ekman variability alone. Although it cannot be explained by the Ekman transport, it is the local wind variability that drives the equatorial AMOC fluctuations by exciting low-mode equatorially trapped planetary waves which have natural periods around 4–10 days (Blaker et al. 2021; Bell et al. 2021). Baker et al. (2022) have shown that the existence of these waves along the equator is supported by observations from the TAO mooring array. Due to the short

time scale, this maximum cannot be captured by monthly outputs explaining why it is not retrieved in longer time scale analysis such as Karspeck et al. (2017). Interestingly, Karspeck et al. (2017) showed that a similar maximum is found when using reanalysis datasets, while it is absent in the corresponding runs without data assimilation.

When decomposed into several components—Ekman, barotropic, geostrophic shear, and residual—as introduced in section 2c(1) [Eq. (2)]. We can see that the AMOC is

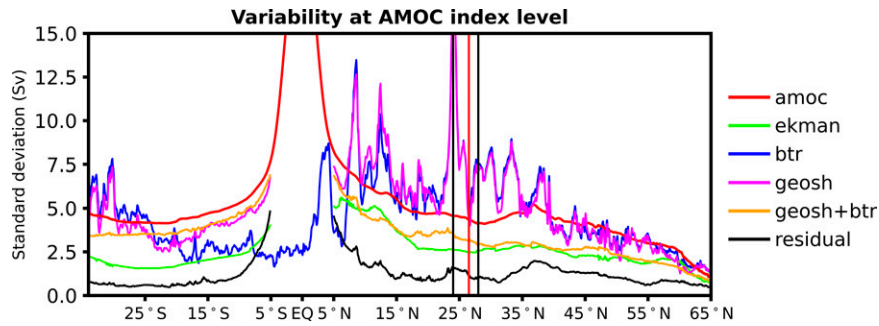


FIG. 3. Time standard deviation of the AMOC index and its components at the depth of the maximum streamfunction. The vertical red line indicates the 26.5°N RAPID array position. The vertical black line indicates 28°N, the latitude for which we show meridional velocity anomalies in Fig. 4.

dominated by the geostrophic shear component in the Southern Hemisphere and northern high latitudes, while Ekman and barotropic components play a major role in northern tropical regions up to approximately 35°N (Fig. 1). As expected, the residual component is small everywhere. The variability of the Ekman component is maximal between 5° and 15°N reflecting the seasonal shift of the intertropical convergence zone in that area (Fig. 2b). It does not vary strongly with the latitude in the rest of the basin. In contrast, the barotropic and geostrophic shear components exhibit large changes of variability depending on the latitudes (Figs. 2c,d). Their variability appears to be stronger in the northern than in the Southern Hemisphere with collocated narrow maxima such as those at 7°N and 24°N. The standard deviation patterns of both components are strikingly similar. The latitudinal variation of the residual component is much smoother, with a first maximum near the equator and a relative maximum between 35° and 40°N.

We define the AMOC index for both strength and variance as the value located at the depth of the time-mean integrated transport identified between 500- and 2000-m depth, to avoid any local shallow maximum. This depth is indicated as a black line in Figs. 1 and 2. The component time series are taken at the same depth to ensure consistency with the relation given in Eq. (2). The variability of these indices as a function of latitude is shown in Fig. 3, summarizing the meridional structure of the component variability observed in Fig. 2. Figure 3 highlights the striking similarity between variability of the barotropic and geostrophic shear components, with collocated spikes of greatly increased variability for certain latitudes. These spikes can exceed 5 Sv within few degrees of latitude such as around 24°N. However, we find that the variability of the sum of these two components (orange line in Fig. 3) is much weaker and smoother (without any spikes), indicating a large degree of compensation between the two components. This is particularly clear for the latitudes that exhibit the spikes in variability mentioned above. Accordingly, a strong negative correlation is found between the two components time series at these specific latitudes such as 24°N where the correlation coefficient reaches -0.98 , which is significant at the 99% confidence level. The compensation between these

two components is likely linked to spatial fluctuations of relatively strong surface currents. For example, when such a current is situated over shallow topography it mainly projects onto the external mode as it will be associated with a high velocity throughout the water column and accordingly a high barotropic velocity. The opposite is true for geostrophic shear transport as the vertical shear is relatively weak. When the surface current shifts offshore where the ocean bottom is much deeper the situation is reversed: The deep ocean means that high velocities are mainly confined to the thickness of the surface current and bottom velocities will typically be low. In this case the surface current increases the vertical velocity shear, hence mainly projecting onto the geostrophic shear transport. For the external mode the opposite is true: the great ocean depth means that even a strong surface current does not result in a high barotropic velocity and hence there is only a weak projection onto the external mode. Thus, the large and strongly anticorrelated variabilities we find for the barotropic and geostrophic components result from an artifact of the decomposition of a much less variable flow (corresponding to the sum of the two). Consistent with this hypothesis, high BTR (GEOSH) anomalies at 28°N are associated with strong (weak) northward Gulf Stream and the associated northward transport further offshore ($\sim 78^\circ\text{W}$) on the shelf (Figs. 4c,d), and weak (high) northward surface Antilles Current offshore ($\sim 75.5^\circ\text{W}$). The combined strong Gulf Stream and weak surface Antilles Currents (Fig. 4c) tend to enhance the barotropic structure of the currents and therefore enhance (decrease) the BTR (GEOSH) transport. Similarly, the large fluctuations found at 24°N are linked with fluctuations of the Loop Current within the Gulf of Mexico (not shown). These compensated fluctuations drop to a local minimum close to 26.5°N (red lines in Figs. 3 and 4a), where the AMOC is monitored by the RAPID-MOCHA array and most of the northward flow is constrained by the Florida Strait. We note here that the compensation is not strong everywhere: between 5°S and about 20°S the variability in the geostrophic component is clearly larger in GEOSH than for BTR. Finally the residual component arising from ageostrophic flow appears to be the weakest contribution to the AMOC variability, but still not negligible.

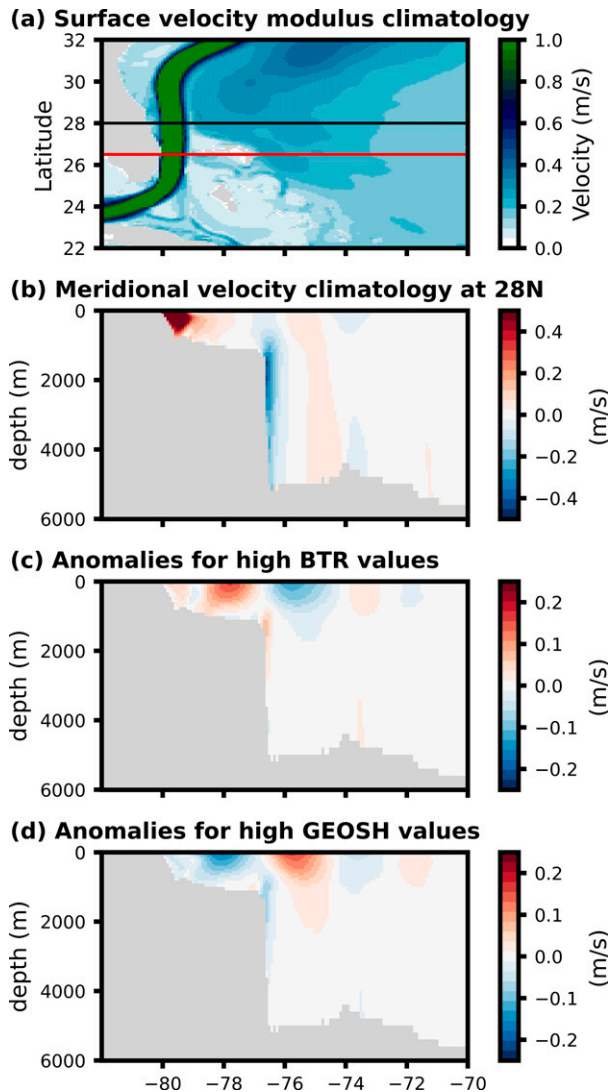


FIG. 4. (a) Surface velocity modulus averaged over the 1960–2012 period. (b) Meridional velocity at 28°N averaged over 1960–2012 period. (c),(d) Meridional velocity anomalies at 28°N coinciding with times when the values of BTR and GEOSH exceed the long-term mean at 28°N by one standard deviation.

b. Chaotic variability

Despite the common atmospheric forcing, and the very close initial states, the oceanic chaotic variability leads the ensemble members to diverge with time (Fig. 5). The ensemble variance $\sigma_m(t)$ of the transport ψ at the time t is calculated as

$$\sigma_m^2(t) = \frac{1}{N_{mb}} \sum_{i=1}^{N_{mb}} [\psi_i(t) - \langle \psi(t) \rangle]^2, \quad (17)$$

where N_{mb} is the ensemble size (i.e., 4), m denotes the ensemble (2007 or 2009), and the angular brackets denote the ensemble mean.

The variance σ_m^2 is a measure for the ensemble spread and increases with time until it saturates and fluctuates around a

constant value (Fig. 5c). The saturation value is taken as the average of the ensemble variance for years 3 and 4 of the integrations of both the ensembles starting in 2007 and 2009 (solid black line in Fig. 5c) and is computed according to

$$\sigma_{\text{SAT}}^2 = \frac{1}{2N_t} \sum_{t=1}^{N_t} [\sigma_{2007}^2(t) + \sigma_{2009}^2(t)], \quad (18)$$

where N_t is the number of 5-day means within two years of integration, i.e., 73×2 and where $\sigma_{2007}^2(t)$ and $\sigma_{2009}^2(t)$ are the ensemble mean variances for the ensembles starting in 2007 and 2009. Stationarity of the internal variance is the underlying assumption for using σ_{SAT}^2 . The variance σ_m^2 varies substantially during the integrations but the average variance over years 3 and 4 (horizontal black line in Fig. 5c) is 1.8 Sv^2 in both ensembles. The phases with higher and lower variances (Fig. 5c) are a consequence of the small ensemble size of 4. For larger ensemble sizes this variability markedly reduces (see appendix). That we find the same value of 1.8 Sv^2 for both ensembles suggests that stationarity of the internal variance is a reasonable assumption.

The ensemble variance can be compared to the total variance of the full long N006 run AMOC time series, hence providing an estimate of the oceanic chaotic variability fraction. This computation can be made for each component of the AMOC to provide insight into the processes involved. We emphasize here that the ensemble size is small in our setup. Therefore we will likely underestimate the ensemble variance linked to chaotic processes. However, we illustrate in appendix that even with $N_{mb} = 4$ our estimate is likely to capture about 3/4 of the variance one would get with a much larger ensemble (Fig. A1).

The full meridional-depth pattern of the ensemble variance saturation value reflects the variability pattern of the AMOC (Fig. 6a). The equatorial region stands out as one of the regions with the lowest fractions of chaotic variability (i.e., the ratio of the ensemble variance saturation value to the N006 variance, Fig. 6b), highlighting the strongly wind-forced characteristic of the variability maximum there. In the North Atlantic, 5°, 24°, and 38°N appear to be the regions with the highest fraction of chaotic AMOC variability (Fig. 6c, red line). In contrast, the subpolar region (i.e., between 45° and 65°N) exhibits a relatively small fraction of chaotic variability, except in the Greenland–Scotland ridge region around 64°N.

Strikingly, the fraction of chaotic variability of the barotropic and geostrophic shear components is much higher than for the total AMOC index fraction, ranging from about 30% to slightly more than 100% for some latitudes (e.g., around 31°N). As with their total variability, this fraction varies strongly with the latitude, and is strongly collocated. It highlights the chaotic nature of the spatial fluctuations of the current pathways accountable for the geostrophic shear and barotropic compensation. As with the total variability, the chaotic variability of the two components strongly compensates one another as indicated by the smaller variance found for the sum between the chaotic components of BTR and GEOSH (Table 2). Additionally, the chaotic fraction of the sum of BTR and GEOSH are much less latitude dependent. In

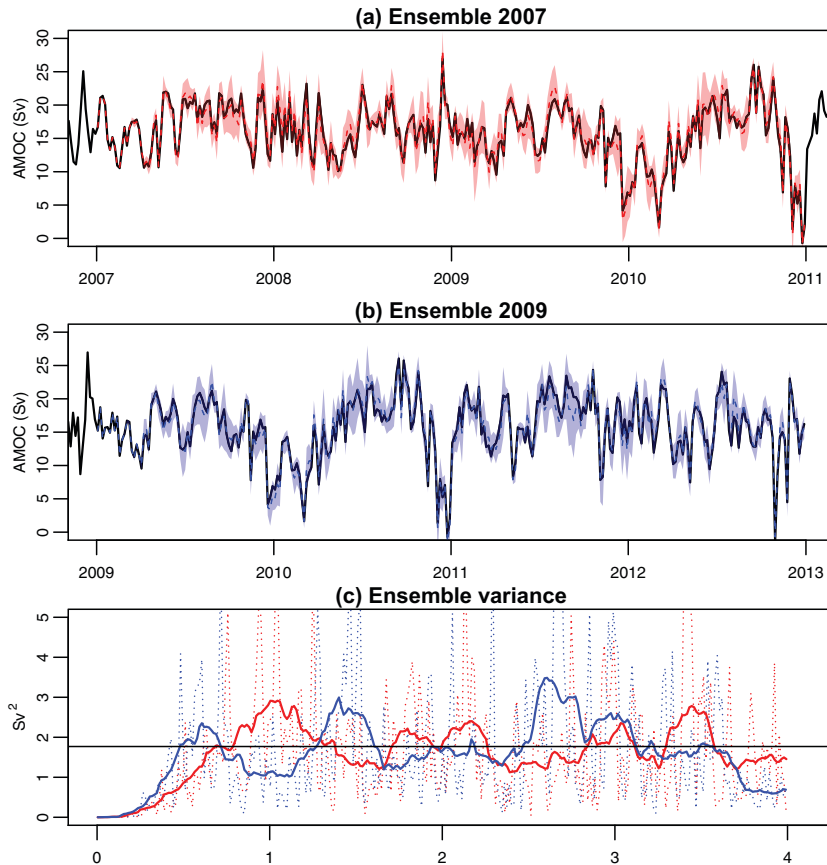


FIG. 5. (a),(b) Full AMOC index time series for the N006 simulation (black line) and the 2007 and 2009 ensemble mean (red and blue lines, respectively). Ensemble spread (one standard deviation) is shown in red and blue shading, respectively. (c) Ensemble variance of the full AMOC as a function of lead time from the starting date for the 2007 (thin red line) and 2009 (thin blue line) ensemble. Thick lines correspond to the running average over a 3-month (seasonal) window. The solid black line indicates the saturation value of the ensemble variance. For both ensembles E2007 and E2009 we average the variances over the last two years and find the same value of 1.8 Sv^2 .

contrast to the total variability, where the compensation between barotropic and geostrophic is weak in the tropical latitudes of the South Atlantic, there is strong compensation at all latitudes for the chaotic variability. The residual component is strongly chaotic, with the same latitude-dependent fluctuation as barotropic and geostrophic shear, likely reflecting topographic changes with latitude as well. However, this chaotic variability corresponds to a weak contribution to the total AMOC transport and variability (Figs. 1e and 2e). As expected, the chaotic fraction of the Ekman component variability is very weak ($<0.1\%$) and is therefore not shown in the figure. Note that all these estimations are computed from 5-day means. When repeating these using annual means (not shown), it appears that the saturation of the ensemble spread is not reached yet.

We note that is also true for 5-day means but the dominance of the chaotic variability by short time scales (e.g., Hirschi et al. 2013) means that the saturation value we find

based on 5-day averages is close to the chaotic variability we would find in longer simulations. The chaotic fraction of variability assessed here is mainly due to subannual variability. Estimating the fraction of chaotic variability for interannual and longer time scales would require longer integrations and cannot be assessed with our experiments.

To summarize, the fraction of chaotic variability of the AMOC varies between 3% and 26% depending on the latitude. When considering the AMOC decomposition into barotropic and baroclinic components, it appears that small chaotic fluctuations in the position of currents account for a strong compensation between the variability of the barotropic and geostrophic shear components at subannual time scale.

4. The AMOC at 26.5°N

The full AMOC decomposition [Eq. (2)] analyzed in the previous section is not exactly the one used in the RAPID

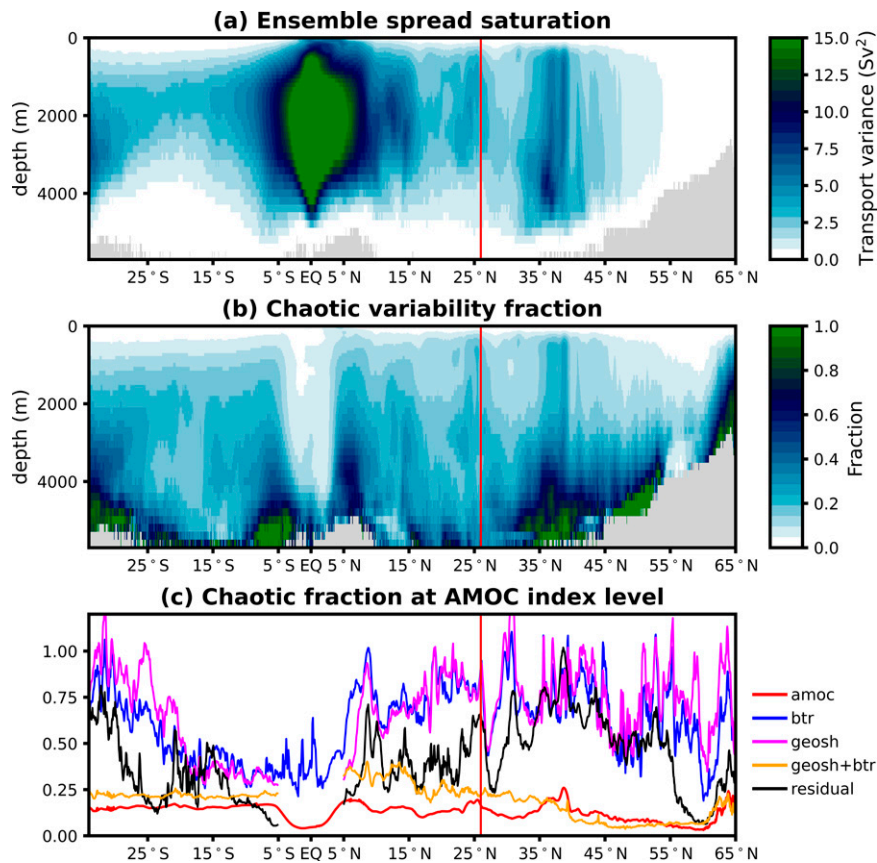


FIG. 6. (a) Ensemble variance saturation value (see Fig. 5 for details) and (b) chaotic variability fraction, for the zonal mean streamfunction. (c) Chaotic variability fraction for the AMOC index and its components at the same depth level [black horizontal curve in (a) and (b)]. The red vertical line highlights the RAPID–MOCHA array position at 26.5°N.

array as it assumes perfect knowledge of the external (barotropic) mode. A key finding of the previous section is that (by construction) for both the geostrophic and barotropic components the chaotic variability can be much larger than for the AMOC. This raises the question whether not being able to “perfectly” observe the external mode may result in an artificial AMOC variability arising from a reduced compensation between the geostrophic and barotropic variability. As shown in section 3, perfect knowledge of the external mode means that the variability in both components largely cancels out. In this section we therefore want to establish to what extent this is still true when using assumptions underlying the RAPID observations at 26.5°N. To answer this question, we investigate the influence of the chaotic variability on the reconstructed AMOC ψ_R as assessed following the RAPID array methodology [Eq. (16) in section 2c(2)].

a. Total variability

To evaluate the ability of the ORCA12 N006 simulation to reproduce the characteristics of the observed AMOC variability at 26.5°N we compare the components of the RAPID-like reconstruction [ψ_R in section 2c(2)] and its components—

Ekman, Florida Strait (FS), and UMO—with the corresponding time series in the RAPID–MOCHA array observations (Fig. 7). The model slightly underestimates the AMOC strength (by 1 Sv) and variability (by 0.4 Sv) but there is reasonable agreement between the simulated and observation-derived time series. There is a high level of correlation between the two time series (0.69), and this is almost unchanged after a linear detrend (see Table 1). The presence of chaotic variability (in both the model and the real world) means that one cannot expect the model to exactly reproduce the observed variability. Even with a “perfect” model and exactly known surface forcing the correlation with observations would never be unity as this would require the spatio-temporal distribution of all dynamical processes in the ocean, including mesoscale and submesoscale eddies, and the phases of internal waves, to exactly match those of the real ocean.

As expected, the agreement for the Ekman component is very high, reflecting the highly forced nature of this component, with almost no impact of the oceanic variability. In contrast, the correlation between the simulated and observed FS and UMO are low (see Table 1). This likely reflects a combination of the model’s limitation in simulating the observed transports as well

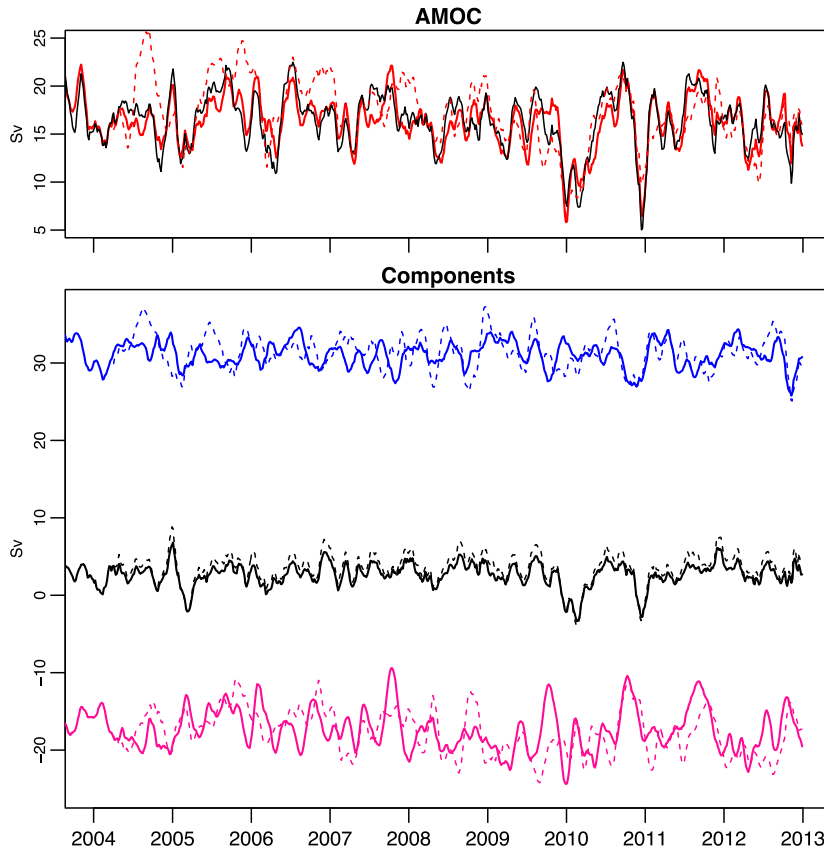


FIG. 7. AMOC, RAPID-like reconstructed AMOC time series and its components for the N006 simulation. (top) AMOC (black solid), reconstructed AMOC (red solid) and RAPID-MOCHA array (red dashed line) over the period 2004–12. (bottom) Blue, black, and magenta lines correspond to the Florida Strait (blue), Ekman (black), and the upper midocean (magenta) transports, respectively. Dashed lines are the components from the RAPID-MOCHA array. All time series are smoothed by a one-month running average.

as a more important role of internal variability for these components.

b. Chaotic variability

Chaotic variability estimation of the RAPID-like reconstructed AMOC ψ_R and its components (FS and UMO) are shown in Table 2. The ψ_R chaotic fraction is found to be slightly higher (15%) than for the full AMOC (10%, when excluding the Gulf of Mexico, Table 3). The main contribution of the chaotic variability arises from the FS transport (35%), which is partly compensated by the UMO chaotic variability. As detailed in section 2c, in this decomposition, part

TABLE 1. Correlation coefficients between observed and simulated time series over the common period 2004–12 for time series smoothed with a 1-month running average (Fig. 7).

	AMOC	UMO	FS	Ekman
Raw	0.69	0.43	0.43	0.97
Detrended	0.70	0.43	0.42	0.97

of the barotropic component is included in the FS transport, another part arising from the density differences at boundaries is included in the UMO component, but the part arising from local barotropic velocity across the main basin is lost. The part of the barotropic transport included in the UMO component plays an important role in the estimation of the chaotic variability. Indeed, when considering the third decomposition (ψ_{R-B}) where the barotropic component is removed from the UMO component in the main basin, the chaotic variability fraction of the AMOC variability rises to 22%, which corresponds to an overestimation by a factor 2 (see Table 2). Hence, the fraction of the barotropic component assessed from the FS transport is not sufficient to retrieve the compensation of chaotic variability between the barotropic and geostrophic shear components. Despite this lack of compensation, the RAPID-MOCHA array gives a reasonably good estimation thanks to the fraction of the barotropic transport included in UMO as a consequence of the assumption of a level of no motion at 4820 dbar (McCarthy et al. 2015), which is essentially equivalent to assuming a

TABLE 2. Total, chaotic, and chaotic fraction of the reconstructed AMOC variance (Sv^2) and its components at $26.5^\circ N$. $AMOC_R$ corresponds to the reconstructed AMOC following the description of section 2c(2), i.e., using the main basin geostrophic compensated component (UMO_R), while $AMOC_{R-B}$ corresponds to the reconstructed AMOC detailed in section 2c(3), i.e., using the main basin geostrophic shear (UMO_{R-B}) component. The Florida Strait transport (FS) is similar for both decompositions.

	Chaotic variance	Total variance	Chaotic fraction
FS_R	2.4	6.9	35%
UMO_R	3.4	10.9	31%
UMO_{R-B}	5.0	10.9	45%
$(FS + UMO)_R$	2.2	8.8	25%
$(FS + UMO)_{R-B}$	3.9	9.4	42%
$AMOC_R$	2.3	15.4	15%
$AMOC_{R-B}$	3.6	16.5	22%

level of no motion at the bottom as we do for our AMOC reconstructions in the model.

To summarize, the strong compensation of the chaotic variability between the barotropic and geostrophic shear components highlighted in the previous section still applies for the corresponding RAPID array components (i.e., FS and UMO). However, part of the barotropic component arising from local barotropic velocity in the main basin is lost, implying that part of the chaotic variability of the geostrophic shear component is not compensated anymore. As a result, the AMOC chaotic fraction is slightly overestimated by the RAPID array reconstruction.

c. The 2009/10 event

Until now we have assessed the chaotic AMOC variability as an average over a period of several years. In a next step we will assess whether the most extreme AMOC event recorded so far by the RAPID observing system in 2009/10 was particular in terms of chaotic contribution.

In 2009/10, the AMOC underwent a transient decline of roughly 30% (Bryden et al. 2014; Srokosz and Bryden 2015). This decline is believed to be partly responsible for the cooling of the subtropical North Atlantic throughout 2010 (Cunningham et al. 2013) with potential impact on the weather over the North Atlantic and European region. Both Roberts et al. (2013) and Blaker et al. (2015) showed that the main features of this event are captured in an ensemble of forced ocean simulations, suggesting that the atmospheric forcing played a dominant role in this event.

The 2009/10 slowdown event and the following event in early 2011 are well reproduced in the simulation, both in terms of timing and amplitude (Fig. 7). It is even more striking in the cumulative transports of each component (Fig. 8). The cumulative transport is computed as the cumulative sum of the time series anomalies from April 2004 to the end of the time series. The anomalies are computed from the average for the period from April 2004 to December 2008, which represents the “normal” AMOC following the method described in Bryden et al. (2014). Even though the events seem underestimated in ORCA12 compared to the observations when using the raw data (Figs. 8a,b), this underestimation disappears completely when considering linear detrended data (Figs. 8c,d). This highlights the strong sensitivity of this diagnostic to long-term trends in the time series. A disagreement in the linear trend between two time series, even very small, could end up in a very different behavior of the cumulative transport. Therefore, when analyzing a short-term event such as the AMOC decline in 2009/10 in this way, the long-term trend should be removed for proper comparison. For the results shown in Figs. 8c and 8d, we therefore remove the transport trend for the 2004–12 period in the N006 hindcast. In this case, the agreement is remarkably good for all components. While we expect good model–observation agreement for the Ekman component, this is more surprising for the FS and UMO components. Our results imply that the 2009/10 event can be mostly reconstructed from the forcing alone for the AMOC as well as for its components in accordance with the findings of Roberts et al. (2013).

To characterize the behavior of the chaotic variability of the AMOC during 2009/10, we look at the E2007 ensemble variance during the event (Fig. 9). Note that the assessment of the average chaotic variability (Figs. 5 and 6) takes into account the period covering the 2009/10 event for the E2007 ensemble. However, even though we cannot obtain a robust conclusion from our experiment, the comparison of the ensemble variance fluctuations and the AMOC fluctuations gives a first insight into the contribution of chaotic variability to this extreme event. The E2009 ensemble is also included in Fig. 9b and even though the start date is so close to the onset of the 2009/10 slowdown the spread is similar in both ensembles during the event.

The chaotic variability of the AMOC during the event is very close to the average, with no remarkable behavior of the ensemble variance, either for the AMOC nor its components. The same is true during the following drop in early 2011. Interestingly, the ensemble variance of the full AMOC ψ_{full} , the RAPID-like reconstruction ψ_R and the UMO and FS components are significantly (at the 95% confident level) above the

TABLE 3. Total, chaotic, and chaotic fraction of the full AMOC variance (Sv^2) at $26.5^\circ N$ and its barotropic (BTR) and geostrophic shear (GEOSH) components. The transports are computed in the main basin, as done in the RAPID–MOCHA array (i.e., excluding the Gulf of Mexico).

	BTR	GEOSH	BTR + GEOSH	RES	AMOC
Chaotic variance (Sv^2)	3.9	4.6	1.8	0.1	1.8
Total variance (Sv^2)	9.8	10.1	9.8	0.4	17.7
Chaotic fraction	40%	45%	19%	32%	10%

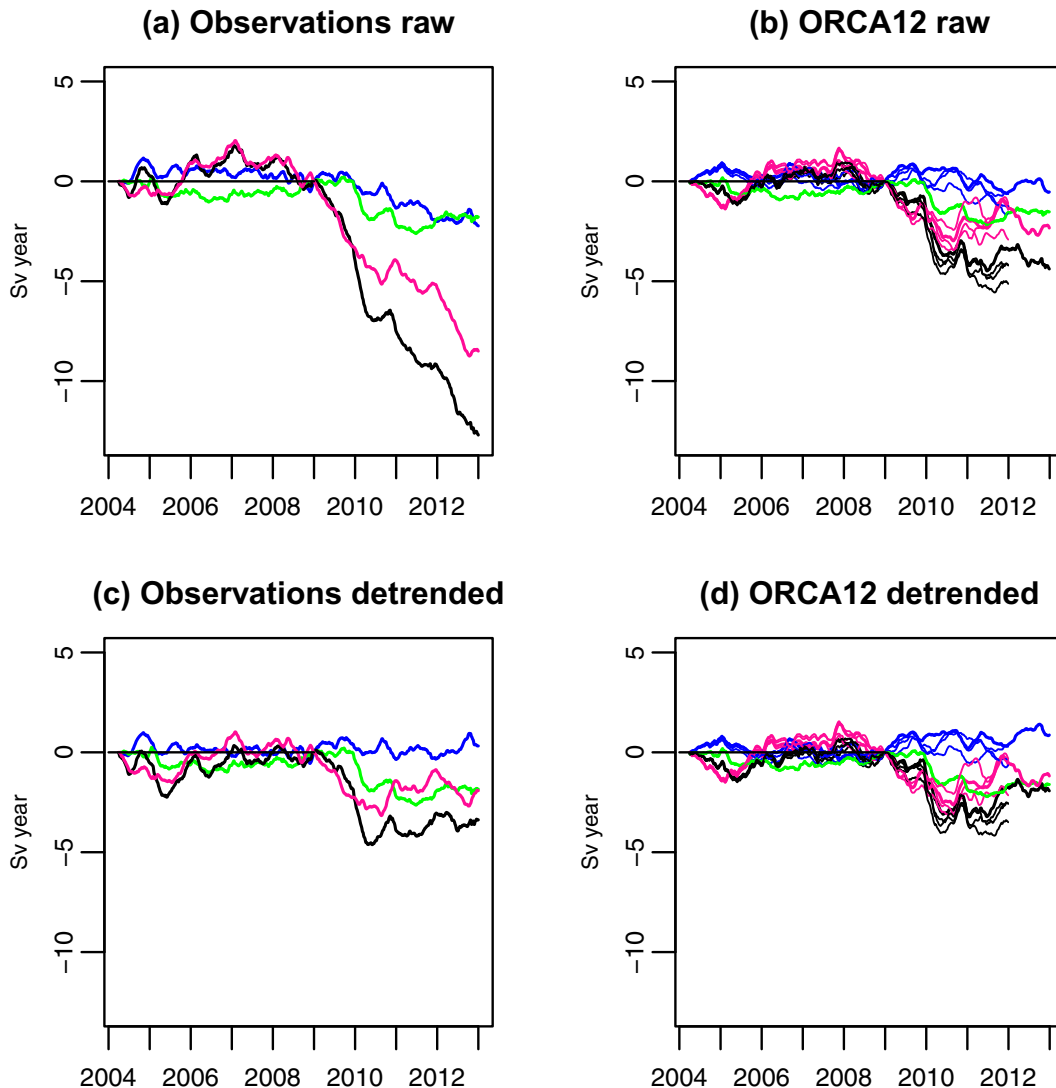


FIG. 8. Cumulative transport anomalies over the RAPID–MOCHA period (a),(c) in the observations and (b),(d) in the model simulations for (top) raw time series and (bottom) linearly detrended time series. The transport anomalies are computed with respect to normal conditions, which are defined to be the average over the 2004–08 period following the approach of Bryden et al. (2014). Then, the anomalous transport is accumulated over time. Line colors: AMOC (black), Florida Straits (blue), Ekman (green), and upper midocean (magenta). Thick and thin lines in (b) and (c) show the AMOC and its components for the control simulation N006 and for the additional 3 ensemble members, respectively.

average in late 2011. This remarkable increase in the chaotic variability is reproduced in the E2009 ensemble (not shown) for the full AMOC ψ_{full} and the UMO component, but weaker and delayed by 3 months, and is not retrieved for the FS component and the reconstructed AMOC ψ_R . It does not correspond to any remarkable event in the AMOC or its components fluctuations and therefore is not straightforward to understand.

In summary, the 2009/10 event is very well reproduced in ORCA12, suggesting a dominant role of the atmospheric forcing. This event does not stand out in terms of chaotic variability with a value which remains close to the average of the 2008–12 period. The idealized model used in the appendix

(Figs. A1, A2) suggests, that for an ensemble size of 4, events such as in 2011 (Fig. 9b) are not uncommon but that these no longer stand out when the ensemble size is increased (Fig. A2).

5. Discussion and conclusions

The chaotic variability of the full AMOC exhibits local maxima around 24°, 38°, and 64°N. The first two peaks, around 24° and 38°N, respectively, have already been observed for interannual to decadal chaotic variability of the AMOC by Leroux et al. (2018, their Fig. 4b), showing that

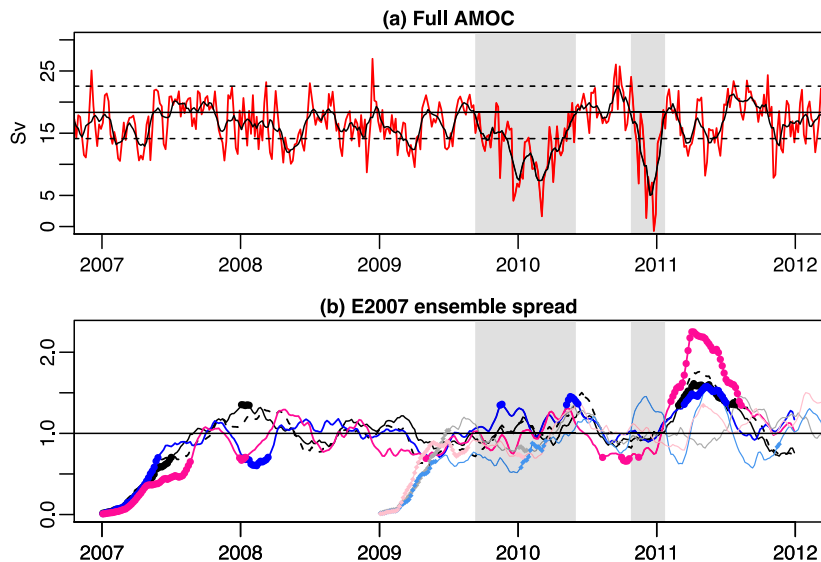


FIG. 9. (a) RAPID-like reconstructed AMOC time series as simulated in N006 from 5-day means (red line) and one-month running mean (black line). (b) E2007 and E2009 ensemble standard deviations for the AMOC and its components normalized by their respective standard deviations. Solid black: saturation value of the AMOC. Black dashed: AMOC-R. Solid magenta: upper midocean. Solid blue: Florida Strait component. The respective color dots (E2007) and squares (E2009) highlight values, which are significantly different from one according to a Fisher test at the 95% confidence level. The time series are smoothed by a seasonal (3 month) running mean. The gray shading highlights the 2009/10 minimum event and the associated second minimum in 2010/11 (Blaker et al. 2015).

these latitudes stand out as relatively chaotic on a large range of time scales. However, the processes responsible for these local maxima remain unclear, as they do not correspond to specific maxima in the chaotic variability of the AMOC components. Note that the Loop Current in the Gulf of Mexico might be a good candidate to explain the peak around 24°N. Indeed, it has been found to account for a particularly strong compensated variability of both the barotropic and geostrophic shear contributions at this latitude (not shown). In addition to this compensated variability, part of the Loop Current fluctuations is likely to impact the AMOC transport at this latitude, thereby increasing its chaotic behavior (Hirschi et al. 2020). The peak at 38°N is likely related to the eddy activity around the separation of the Gulf Stream and its extension into the North Atlantic drift.

A striking feature in our findings is the large, often compensating variability in the barotropic and geostrophic shear contributions. Since any temporally variable or constant transport (or any time series) can in principle be decomposed into two large, compensating transports, this variability is somewhat artificial. However, in our case the decomposition into the barotropic and geostrophic shear components provides insight into the nature of the chaotic AMOC transport variability. The high fraction of chaotic variability for BTR and GEOSH (Fig. 6) indicates that there is a higher degree of decorrelation between ensemble members than for the other AMOC components. For example, assuming a case where the correlation is zero one can expect to find a chaotic variability

fraction of 1. While eddies cannot explain the total variability seen for BTR and GEOSH (Table 2) they are characterized by strong barotropic and geostrophic velocities which are decorrelated between ensemble members. Hence one can expect the differences between ensemble members to sometimes be large. Additionally, the small number of ensemble members (4) can lead to an overestimate of the variability (in the same way as one can overestimate the variance of, e.g., a long time series when estimating the variance of the full time series from one small subsample). This can be seen in Fig. A1, which illustrates that even though the average variance is underestimated with an ensemble size of 4, there are instances where variance is markedly overestimated. The spikes in chaotic fraction for BTR and GEOSH that exceed 1 seen at some latitudes in Fig. 6 have to be considered in this context.

At 64°N, a maximum of the of the barotropic and geostrophic shear chaotic variability is observed, suggesting that these two components explain most of the relatively high level of chaotic behavior of the AMOC in this region. This peak of chaotic variability has been seen in a 1/4° resolution model simulation by Hirschi et al. (2013) on subannual time scales, but not on interannual time scales, suggesting that this high chaotic variability at subpolar latitudes is restricted to subannual time scales. Consistently, this high chaotic variability is not retrieved in Leroux et al. (2018), who focus on interannual variability. This chaotic behavior at 65°N raises questions about the attribution of recently observed AMOC signal within the OSNAP framework (Holliday et al. 2018; Lozier

et al. 2019). More generally, most of the AMOC chaotic variability arises from the sum of these components, as the Ekman component is strongly forced by the atmosphere. However, the residual component, even though it is a weak contribution to the total AMOC transport exhibits strongly chaotic fluctuations that might have an impact on the chaotic fraction of the AMOC variability.

At 26.5°N the compensated variability of FS and UMO highlighted in our study has been identified in the observations after 2008 (Frajka-Williams et al. 2016), but not during 2004–08 (Kanzow et al. 2010) and is dominated by annual to subannual time scales in accordance with our findings. Note that the chaotic fraction of the AMOC variability might vary with time. The short integration time of our ensemble experiments prevents any investigation of this behavior. However, lack of fluctuation in the ensemble spread over the strong decline observed in 2009–10 suggests that this event does not stand out as remarkable regarding the chaotic variability of the AMOC. Mid-2011 is the only time when our experiments suggest a chaotic variability that markedly differs from the average chaotic variability (Fig. 9b). This indicates that the chaotic AMOC variability may vary in time (i.e., for some periods the AMOC is more “chaotic” than for others). However, the size of our ensemble is too small for us to make a firm statement. With four members the ensemble variance is characterized by spikes (Fig. 5c, Fig. A1) with values much higher than the average variance. The conceptual model used in appendix to illustrate the impact of the ensemble size suggests that at least 10 (but ideally more) ensemble members are needed to determine whether high values such as those seen in mid-2011 in Fig. 9b reflect an increased chaotic variability during that period rather than an artifact of the limited ensemble size (Fig. A2).

In summary, our study has provided a full description of the intra to interannual variability of the AMOC and of its barotropic, geostrophic shear, and Ekman contributions using an eddy-resolving ocean hindcast over the 1960–2012 period. The part of the AMOC variability emerging from chaotic processes such as eddies and waves has been assessed from two ensemble experiments starting in 2007 and 2009, respectively. The main findings of our study are as follows:

- Apart from a very high variability around the equator related to surface wind, the full AMOC variability exhibits its maximum around 35°N, where the standard deviation reaches roughly 5 Sv.
 - The barotropic and geostrophic components each exhibit a large variability (typically 5–8 Sv, with peaks of more than 10 Sv) with a strong compensation between both components. The standard deviation of their sum is roughly 3–4 Sv in the midlatitude North Atlantic, which is similar to the variability due to the Ekman component.
 - The compensation between the barotropic and geostrophic components arises from chaotic spatial fluctuations of specific currents over topography, resulting in the flow mainly projecting on one component or the other.
 - The chaotic fraction of the AMOC variability ranges from 3% to 26% of the total variance, depending on the latitude,
- showing that on intra-annual time scales the AMOC fluctuations in a forced eddy-rich ocean model mainly reflect the prescribed atmospheric variability.
- At 26.5°N, 10% of the total AMOC variance is chaotic. This fraction is slightly overestimated (~15% of the total AMOC variability) by the RAPID methodology owing to the loss of information from the local barotropic velocity in the main basin, which cannot be assessed from the measurements. As a result, part of the geostrophic shear component chaotic variability is not compensated anymore, thereby increasing the estimate of the relative importance of chaotic variability of the AMOC.
 - At 26.5°N, where the AMOC has been monitored daily by the RAPID–MOCHA array since April 2004, the compensated variability of the barotropic and geostrophic shear components is strong (albeit weaker than at most other mid- to high latitudes). This compensated variability is partially retrieved between the RAPID–MOCHA observed contributions, i.e., FS and UMO components.
 - Despite being common to all members the 2009/10 slowdown of the AMOC is not reflected in the ensemble spread compared to values from the 2007–12 period.

Acknowledgments. We thank two anonymous reviewers for their helpful comments which have greatly improved our manuscript. This work was part of the NERC funded project DYNAMOC (NE/M005097/1). JH, AB, and BS also acknowledge funding from the NERC projects MESOCLIP (NE/K005928/1) and ACSIS (NE/N018044/1). This work used the ARCHER U.K. National Supercomputing Service (<http://www.archer.ac.uk>).

Data availability statement. The code and data required to reproduce the work presented in the paper are accessible at Germe et al. (2022).

APPENDIX

Ensemble Size

Our results are based on an ensemble size of only 4 members. The consistency of results seen in earlier studies of the chaotic-AMOC variability using very small, i.e., 2 (Hirschi et al. 2013), or much larger numbers of ensemble members (e.g., 50 in Leroux et al. 2018) provides some confidence that the results we presented in the previous sections are robust. Nevertheless, it is clear that an ensemble size of 4 is not sufficient to accurately capture the full range of chaotic variability. However, even with current HPC resources the generation of a large ensemble with a model such as ORCA12 is prohibitively expensive. In the following we therefore introduce a conceptual model to illustrate how much the small ensemble size used in our study is likely to affect the ensemble variance as well as the time needed for the ensemble spread to reach saturation (Fig. A1). Starting from the AMOC time series (*A*) in one of the ORCA12 ensemble E2007 we construct ensembles of

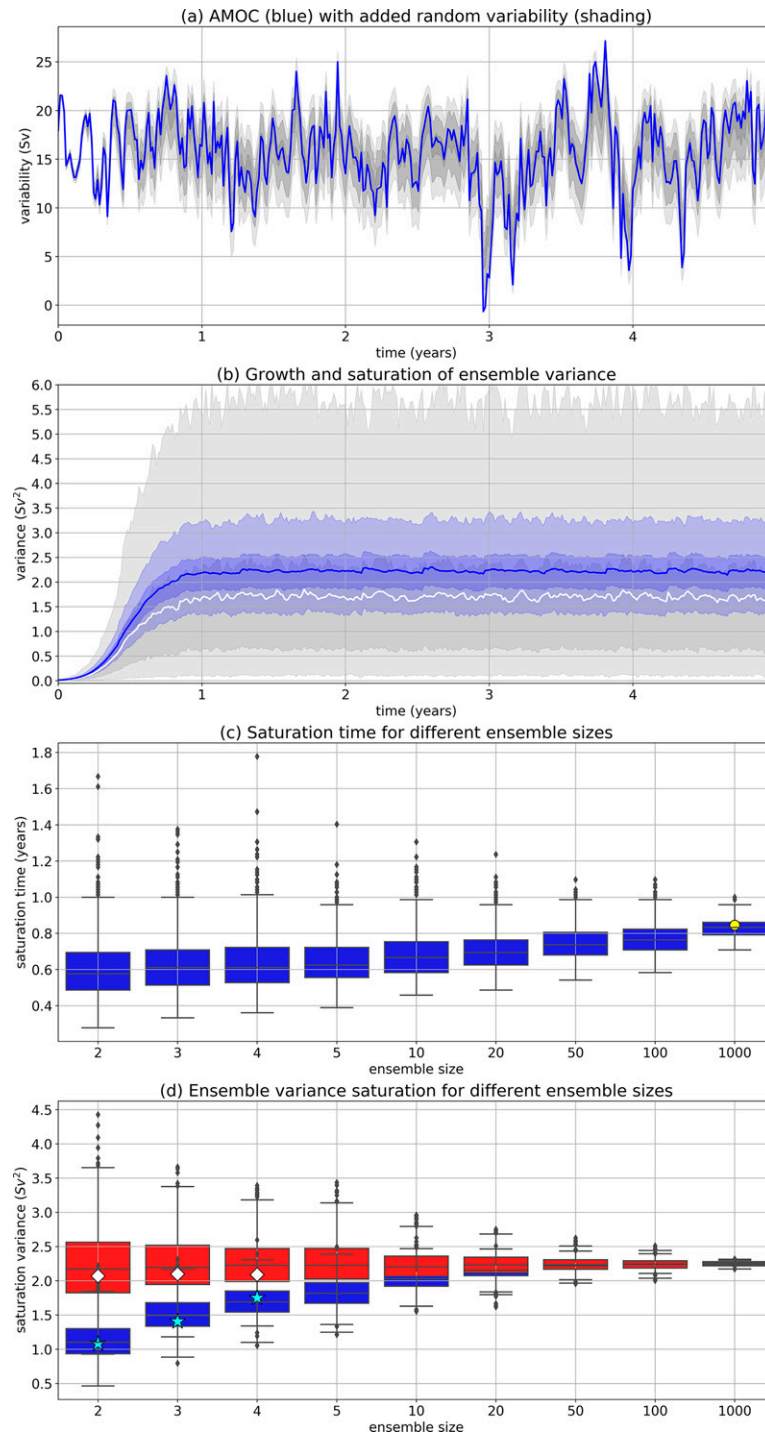


FIG. A1. Impact of ensemble size on estimates of the ensemble variance and of the time needed for the divergence between ensemble members to reach saturation. (a) Envelope from 1000 synthetic ensemble members (gray shading: 2.5, 25, 75, 97.5 percentiles) and AMOC from one of the E2007 ORCA12 ensemble members (blue line). (b) Growth and saturation of ensemble variance during ensemble divergence. Mean ensemble variance for ensemble sizes 4 (white line) and 50 (blue line) calculated following Eq. (A6). Light (dark) gray shading indicates the 2.5 (25) and 97.5 (75) percentiles for ensemble size 4. Light (dark) blue shading: as above but for ensemble size 50. (c) Distribution of saturation time as a function of ensemble size. The yellow circle indicates the actual saturation time. (d) Boxplot of distribution of mean ensemble variance calculated according to Eqs. (A4) (blue) and (A7) (red). Ensemble variances obtained using either Eq. (A4) or (A7) are shown for sizes 2, 3, and 4 (stars and diamonds, respectively).

size $n_k = [2, 3, 4, 5, 10, 20, 50, 100, 1000]$ from artificial time series $\psi_{k,l}(t_i)$:

$$\psi_{k,l}(t_i) = \frac{A'(t_i) + \varepsilon_{k,l}(t_i)f(t_i)}{\sqrt{1 + \frac{\sigma(\varepsilon_{k,l})}{\sigma(A)} f(t_i)}} + \bar{A}, \quad k = [1, \dots, n_k], \quad l = [1, \dots, n_l]. \tag{A1}$$

The time series A is separated into its time-fluctuating and time-mean components $A(t_i) = A'(t_i) + \bar{A}$. $A(t)$ provides a baseline variability common to all ensemble members and in our case it is also common across all ensembles. To generate ensembles we add multiple realizations of the chaotic variability, $\varepsilon_{k,l}(t_i)$, which can also be described as colored noise, which has similar statistical properties (amplitude and autocorrelation) as in our ORCA12 simulations. To obtain $\varepsilon_{k,l}(t_i)$ we use block bootstrapping (Künsch 1989). In a first step we compute differences between ORCA12 ensemble members $p, q = [1, 2, 3, 4]$ from E2007:

$$\Delta\psi_{m,E2007}(t_i) = \psi_{E2007,p}(t_i) - \psi_{E2007,q}(t_i). \tag{A2}$$

$$f(t_i) = \frac{1}{1 + e^{-x}}, \quad x = \left(\frac{at_i}{t_n}\right) - b, \quad t_{i=1,\dots,n} = [0, 5, 10, \dots, 1825], \quad a = 35, \quad b = 3, \tag{A3}$$

with time steps $\Delta t = t_{i+1} - t_i = 5$ days. The denominator $\sqrt{1 + \left[\frac{\sigma^2(\varepsilon_{k,l})}{\sigma^2(A)}\right]f(t_i)}$ in Eq. (A1) ensures that when adding the noise $\varepsilon_{k,l}(t_i)$ the variance of the time series $\psi_{l,k}(t_i)$ does not increase (which it otherwise would) and $\sigma^2(\varepsilon_{k,l})/\sigma^2(A)$ is the ratio between the standard deviations of $\varepsilon_{k,l}(t_i)$ and A . Each ensemble of size n_k is repeated $n_l=1000$ times.

As illustrated in Fig. A1a the statistical model introduced above can be used to simulate a situation where ensemble members diverge while all having a large fraction of total variability in common (similar to what is shown in Figs. 5a,b).

Following Eq. (18) the ensemble variance can then be calculated according to

$$\sigma_{l,k}^2(t_i) = \frac{1}{n_k} \sum_{i=1}^{n_k} \left[\psi_{l,k}(t_i) - \overline{\psi_{l,k}} \right]^2, \tag{A4}$$

$$n_k = [2, 3, 4, 5, 10, 20, 50, 100, 1000].$$

Since for each ensemble size n_k the process is repeated 1000 times we obtain a distribution of values for the ensemble spread (Figs. A1b,d). The saturation time t_s (Fig. A1c) is defined as the time when the ensemble divergence first exceeds $c \overline{\sigma_{l,k}^2(t_i)}$ where $c = 0.9$, and where the overbar denotes the mean over the second half of the time series when saturation has been reached (i.e., t_i between 1000 and 1825 days). Figure A1c illustrates that for small ensemble sizes the saturation time t_s systematically underestimates the true value t_s^* which in this idealized model can readily be determined from the sigmoid function in Eq. (A3). Since we look at the saturation time for the ensemble variance, t_s^* is reached when

This provides a set of 6 time series $\Delta\psi_m$ to inform the statistical properties required for the time series $\varepsilon_{k,l}(t_i)$. By randomly sampling (with replacement) the time series $\Delta\psi_{m,E2007}$, in blocks of sufficient length one gets the new time series $\psi_{k,l}(t_i)$ needed for the bootstrapping. We tested block lengths between 30 and 180 days (i.e., blocks of 6 and 36 time steps) and found a good agreement between the autocorrelations of the synthetic time series and those found for $\Delta\psi_{m,E2007}$ for a block length of 155 days (31 time steps). We note here that the following results about ensemble spread and saturation do not depend strongly on the choice of the block length but remain qualitatively the same for any given window length [and indeed when using different approaches to generate the noise $\varepsilon_{k,l}(t_i)$].

To represent a gradual divergence between the ensemble members, $\psi_{l,k}(t_i)$, a sigmoid function scales the amplitude of $\varepsilon_{k,l}(t_i)$ which is added to the AMOC from ≈ 0 at t_1 to ≈ 1 at t_n :

$$\left(\frac{1}{1 + e^{-x}}\right)^2 = c$$

Solving for x then allows us to determine t_s^* :

$$2e^{-x} + e^{-2x} = \frac{1 - c}{c}, \quad u = e^{-x},$$

$$u^2 + 2u - \frac{1 - c}{c} = 0, \quad u = \frac{-2 + 2\sqrt{\frac{1-c}{c}}}{2},$$

$$x = -\ln(u) = \left(\frac{at_s^*}{t_n}\right) - b,$$

$$t_s^* = \frac{t_n[-\ln(u) + b]}{a},$$

which yields $t_s^* \approx 309$ days (or 0.85 years). Figure A1c illustrates that despite t_s underestimating the saturation time the values obtained for small ensemble sizes are quite close to the actual saturation time t_s^* suggesting that the saturation time found in the ORCA12 ensemble is likely to be a reasonable estimate.

Equation (A4) describes the approach used to estimate the ensemble spread in our ORCA12 ensembles which is the same as in Leroux et al. (2018). As shown in Hirschi et al. (2013), for variability with periods that are short compared to the length of the simulation, the ensemble variance can also be estimated from the difference between pairs of ensemble members:

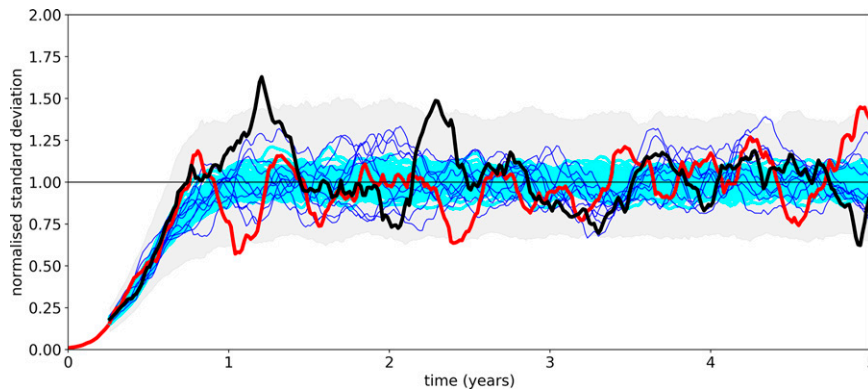


FIG. A2. Normalized ensemble standard deviation (following Fig. 9b) for ensemble sizes of 4 (red and black lines), 10 (blue), and 50 (cyan). Time series are smoothed with a 3-month running mean. Gray shading is the range between the 2.5 and 97.5 percentiles for ensemble size of 4.

$$\psi'_{l_{ij},k} = \left(\psi_{l_{ij},k} - \psi_{l_{ij},k} \right) / \sqrt{2} \quad (\text{A5})$$

$$\sigma_{l_{ij},k}^2 = \frac{1}{t_n - t_s} \sum_{t_i=t_s}^{t_n} \left[\psi_{l_{ij},k}(t_i) - \overline{\psi_{l_{ij},k}} \right]^2, \quad (\text{A6})$$

where the overbar denotes the average of $\psi_{l_{ij},k}(t_i)$ between the saturation time t_s and the last time step t_n . With this approach the temporal information about the ensemble variance as shown in Fig. A1b or Fig. 5 is lost. Equation (A6) cannot be used to estimate how large the ensemble spread is for a particular event. However, it has the advantage that an estimate of the mean ensemble spread can be obtained from only two ensemble members. For each ensemble of size n_k the ensemble variance according to Eq. (A6) is calculated $(n_k - 1)n_l$ times to get a distribution of values. It is instructive to illustrate the differences between calculating the mean ensemble variance according to Eq. (A6) and the mean variance $\overline{\sigma_{l,k}^2}$:

$$\overline{\sigma_{l,k}^2} = \frac{1}{t_n - t_s} \sum_{t_i=t_s}^{t_n} \sigma_{l,k}^2(t_i). \quad (\text{A7})$$

Figure A1d illustrates how the mean ensemble divergence according to Eqs. (A4) and (A7) compare for different ensemble sizes. For small ensemble sizes (A4) underestimates the variance of the ensemble spread but the values obtained with both approaches converge to the same value for increasing ensemble sizes (Fig. A1d). There is little dependence of mean ensemble variance on the ensemble size when using (A7). For small ensemble sizes there is a larger spread of values for the mean variance but the median (and mean) of the distributions is similar for ensemble sizes from 2 to 1000.

With an ensemble size of $n = 4$ (as in our ORCA12 ensemble) our simple model suggests that one is likely to capture about 3/4 of the mean ensemble variance when using Eq. (A4) (Fig. A1d). Figure A1d shows that applying Eqs. (A4) and (A7) for ensemble sizes of 2, 3, and 4 on the ORCA12 data leads to values that fall well within those

from the statistical model calculated. However, as illustrated in Fig. A1b when looking at the ensemble variance for any given point in time the uncertainty is much larger as shown by the spikes in the variance values shown in Fig. 5 and by the high values of the 97.5 percentile in Fig. A1b.

Figure A2 illustrates how the standard deviation of the ensemble standard deviation normalized by its saturation value varies in time for different ensemble sizes. This is equivalent to what is shown for ensemble E2007 in Fig. 9b for the AMOC and its components. Figure A2 suggests that the high values seen in the first half of year 2011 in E2007 are statistically significant as the value of about 1.7 seen for the AMOC in Fig. 9b clearly exceeds the 97.5 percentile of the values obtained for an ensemble size of 4. This could be interpreted as a time varying amplitude of the chaotic variability. However, it is expected that at times the statistical significance levels will be reached by chance. This is illustrated for two 4-member ensembles (Fig. A2, black and red lines) where in one case the 97.5 percentile level is similarly exceeded after about 1.2 and 2.3 years as for the AMOC in E2007 (Fig. 9b). For such a peak to be indicative of a statistically significant temporal change in the amplitude of the ensemble spread one would expect the level of the 97.5th percentile to increase. This, however, is not the case in our statistical model and the peaks at 1.2 and 2.3 years do not mean there is a statistically significant shift in the amplitude of chaotic-intrinsic variability. Whether this would be the case in E2007 cannot be answered—only a larger ensemble size (or a more detailed analysis of e.g., the temporal variability of the mesoscale eddy field in E2007) would tell. Increasing the ensemble size to 10 (blue lines) and 50 (cyan) markedly decreases the amplitude of the excursions for the standard deviation as one expects for randomly distributed ensemble members with no systematic variability in timing of the occurrence of peaks and troughs. In summary, our statistical model illustrates that with an ensemble size of 4 one has to be careful when making statements about the temporal variability of the ensemble spread. However, our statistical model also suggests that

with an ensemble size of 4 one is likely to capture about 3/4 of the average ensemble spread.

REFERENCES

- Alexander-Turner, R., P. Ortega, and J. I. Robson, 2018: How robust are the surface temperature fingerprints of the Atlantic Overturning Meridional Circulation on monthly time scales? *Geophys. Res. Lett.*, **45**, 3559–3567, <https://doi.org/10.1029/2017GL076759>.
- Baker, L. E., M. J. Bell, and A. T. Blaker, 2022: TAO data support the existence of large high frequency variations in cross-equatorial overturning circulation. *Geophys. Res. Lett.*, **49**, e2021GL096879, <https://doi.org/10.1029/2021GL096879>.
- Bell, M. J., A. T. Blaker, and J. J. Hirschi, 2021: Wind-driven oscillations in meridional overturning circulations near the equator. Part II: Idealized simulations. *J. Phys. Oceanogr.*, **51**, 663–683, <https://doi.org/10.1175/JPO-D-19-0297.1>.
- Blaker, A. T., J. J.-M. Hirschi, B. Sinha, B. de Cuevas, S. Alderson, A. Coward, and G. Madec, 2012: Large near-inertial oscillations of the Atlantic meridional overturning circulation. *Ocean Modell.*, **42**, 50–56, <https://doi.org/10.1016/j.ocemod.2011.11.008>.
- , and Coauthors, 2015: Historical analogues of the recent extreme minima observed in the Atlantic meridional overturning circulation at 26°N. *Climate Dyn.*, **44**, 457–473, <https://doi.org/10.1007/s00382-014-2274-6>.
- , J. J. Hirschi, M. J. Bell, and A. Bokota, 2021: Wind-driven oscillations in the meridional overturning circulation near the equator. Part I: Numerical models. *J. Phys. Oceanogr.*, **51**, 645–661, <https://doi.org/10.1175/JPO-D-19-0296.1>.
- Brodeau, L., B. Barnier, A. M. Treguier, T. Penduff, and S. Gulev, 2010: An ERA40-based atmospheric forcing for global ocean circulation models. *Ocean Modell.*, **31**, 88–104, <https://doi.org/10.1016/j.ocemod.2009.10.005>.
- Bryden, H. L., A. Mujahid, S. A. Cunningham, and T. Kanzow, 2009: Adjustment of the basin-scale circulation at 26°N to variations in Gulf Stream, deep western boundary current and Ekman transports as observed by the Rapid Array. *Ocean Sci.*, **5**, 421–433, <https://doi.org/10.5194/os-5-421-2009>.
- , B. A. King, G. D. McCarthy, and E. L. McDonagh, 2014: Impact of a 30% reduction in Atlantic meridional overturning during 2009–2010. *Ocean Sci.*, **10**, 683–691, <https://doi.org/10.5194/os-10-683-2014>.
- Buchan, J., J. J.-M. Hirschi, A. T. Blaker, and B. Sinha, 2014: North Atlantic SST anomalies and the extreme North Europe weather event of December 2010. *Mon. Wea. Rev.*, **142**, 922–932, <https://doi.org/10.1175/MWR-D-13-00104.1>.
- Buckley, M. W., and J. Marshall, 2016: Observations, inferences, and mechanisms of the Atlantic meridional overturning circulation. *Ann. Rev. Geophys.*, **54**, 5–63, <https://doi.org/10.1002/2015RG000493>.
- Chidichimo, M. P., T. Kanzow, S. A. Cunningham, and J. Marotzke, 2010: The contribution of eastern-boundary density variations to the Atlantic meridional overturning circulation at 26.5°N. *Ocean Sci.*, **6**, 475–490, <https://doi.org/10.5194/os-6-475-2010>.
- Clément, L., E. Frajka-Williams, Z. B. Szuts, and S. A. Cunningham, 2014: Vertical structure of eddies and Rossby waves, and their effect on the Atlantic meridional overturning circulation at 26.5°N. *J. Geophys. Res. Oceans*, **119**, 6479–6498, <https://doi.org/10.1002/2014JC010146>.
- Cunningham, S. A., and Coauthors, 2007: Temporal variability of the Atlantic meridional overturning circulation at 26.5°N. *Science*, **317**, 935–938, <https://doi.org/10.1126/science.1141304>.
- , and Coauthors, 2013: Atlantic meridional overturning circulation slow-down cooled the subtropical ocean. *Geophys. Res. Lett.*, **40**, 6202–6207, <https://doi.org/10.1002/2013GL058464>.
- Dee, D. P., and Coauthors, 2011: The ERA-Interim reanalysis: Configuration and performance of the data assimilation system. *Quart. J. Roy. Meteor. Soc.*, **137**, 553–597, <https://doi.org/10.1002/qj.828>.
- de Verdière, A., and R. Tailleux, 2005: The interaction of a baroclinic mean flow with long Rossby waves. *J. Phys. Oceanogr.*, **35**, 865–879, <https://doi.org/10.1175/JPO2712.1>.
- Duchez, A., E. Frajka-Williams, N. Castro, J. Hirschi, and A. Coward, 2014: Seasonal to interannual variability in density around the Canary Islands and their influence on the Atlantic meridional overturning circulation at 26°N. *J. Geophys. Res. Oceans*, **119**, 1843–1860, <https://doi.org/10.1002/2013JC009416>.
- , P. Courtois, E. Harris, S. A. Josey, T. Kanzow, R. Marsh, D. Smeed, and J.-M. Hirschi, 2016a: Potential for seasonal prediction of Atlantic sea surface temperatures using the RAPID array at 26°N. *Climate Dyn.*, **46**, 3351–3370, <https://doi.org/10.1007/s00382-015-2918-1>.
- , and Coauthors, 2016b: Drivers of exceptionally cold North Atlantic Ocean temperatures and their link to the 2015 European heat wave. *Environ. Res. Lett.*, **11**, 074004, <https://doi.org/10.1088/1748-9326/11/7/074004>.
- Dussin, R., B. Barnier, and L. Brodeau, 2014: The making of Drakkar forcing set DFS5. DRAKKAR/MyOcean Rep. 05-10-14, 29 pp., <https://www.drakkar-ocean.eu/forcing-the-ocean/the-making-of-the-drakkar-forcing-set-dfs5>.
- Fichefet, T., and M. A. M. Maqueda, 1997: Sensitivity of a global sea ice model to the treatment of ice thermodynamics and dynamics. *J. Geophys. Res.*, **102**, 12 609–12 646, <https://doi.org/10.1029/97JC00480>.
- Frajka-Williams, E., and Coauthors, 2016: Compensation between meridional flow components of the Atlantic MOC at 26°N. *Ocean Sci.*, **12**, 481–493, <https://doi.org/10.5194/os-12-481-2016>.
- Gastineau, G., and C. Frankignoul, 2012: Cold-season atmospheric response to the natural variability of the Atlantic meridional overturning circulation. *Climate Dyn.*, **39**, 37–57, <https://doi.org/10.1007/s00382-011-1109-y>.
- Germe, A., J. J.-M. Hirschi, A. T. Blaker, and B. Sinha, 2022: NOC-MSM/CHAMOC: Chaotic variability of the Atlantic meridional overturning circulation at sub-annual time scales (v1.0.1). Zenodo, accessed 8 April 2022, <https://doi.org/10.5281/zenodo.5911238>.
- Grégorio, S., T. Penduff, G. Sérazin, J. M. Molines, B. Barnier, and J. Hirschi, 2015: Intrinsic variability of the Atlantic meridional overturning circulation at interannual-to-multidecadal time scales. *J. Phys. Oceanogr.*, **45**, 1929–1948, <https://doi.org/10.1175/JPO-D-14-0163.1>.
- Hallam, S., R. Marsh, S. A. Josey, P. Hyder, B. Moat, and J. J.-M. Hirschi, 2019: Ocean precursors to the extreme Atlantic 2017 hurricane season. *Nat. Commun.*, **10**, 896, <https://doi.org/10.1038/s41467-019-08496-4>.
- Hirschi, J. J.-M., and J. Marotzke, 2007: Reconstructing the meridional overturning circulation from boundary densities and the zonal wind stress. *J. Phys. Oceanogr.*, **37**, 743–763, <https://doi.org/10.1175/JPO3019.1>.
- , A. T. Blaker, B. Sinha, A. Coward, B. de Cuevas, S. Alderson, and G. Madec, 2013: Chaotic variability of the

- meridional overturning circulation on subannual to interannual timescales. *Ocean Sci.*, **9**, 805–823, <https://doi.org/10.5194/os-9-805-2013>.
- , and Coauthors, 2020: The Atlantic meridional overturning circulation in high resolution models. *J. Geophys. Res. Oceans*, **125**, e2019JC015522, <https://doi.org/10.1029/2019JC015522>.
- Hochet, A., T. Huck, O. Arzel, F. Sévellec, M. Mazloff, B. Cornuelle, and A. Colin de Verdière, 2020: Direct temporal cascade of temperature variance in eddy-permitting simulations of multidecadal variability. *J. Climate*, **33**, 9409–9425, <https://doi.org/10.1175/JCLI-D-19-0921.1>.
- Holliday, N. P., S. Bacon, S. A. Cunningham, S. F. Gary, J. Karstensen, B. A. King, F. Li, and E. L. McDonagh, 2018: Subpolar North Atlantic overturning and gyre-scale circulation in the summers of 2014 and 2016. *J. Geophys. Res. Oceans*, **123**, 4538–4559, <https://doi.org/10.1029/2018JC013841>.
- Jayne, S. R., and J. Marotzke, 2001: The dynamics of ocean heat transport variability. *Rev. Geophys.*, **39**, 385–411, <https://doi.org/10.1029/2000RG000084>.
- Jourdan, D., E. Balopoulos, M. Garcia-Fernandez, and C. Maillard, 1998: Objective analysis of temperature and salinity historical data set over the Mediterranean basin. *OCEANS'98 Conf. Proc.*, Nice, France, Institute of Electrical and Electronics Engineers, 82–87, <https://doi.org/10.1109/OCEANS.1998.725649>.
- Kanzow, T., H. L. Johnson, D. P. Marshall, S. A. Cunningham, J. J.-M. Hirschi, A. Mujahid, H. L. Bryden, and W. E. Johns, 2009: Basinwide integrated volume transports in an eddy-filled ocean. *J. Phys. Oceanogr.*, **39**, 3091–3110, <https://doi.org/10.1175/2009JPO4185.1>.
- , and Coauthors, 2010: Seasonal variability of the Atlantic meridional overturning circulation at 26.5°N. *J. Climate*, **23**, 5678–5698, <https://doi.org/10.1175/2010JCLI3389.1>.
- Karspeck, A. R., and Coauthors, 2017: Comparison of the Atlantic meridional overturning circulation between 1960 and 2007 in six ocean reanalysis products. *Climate Dyn.*, **49**, 957–982, <https://doi.org/10.1007/s00382-015-2787-7>.
- Knight, J. R., R. J. Allan, C. K. Folland, M. Vellinga, and M. E. Mann, 2005: A signature of persistent natural thermohaline circulation cycles in observed climate. *Geophys. Res. Lett.*, **32**, L20708, <https://doi.org/10.1029/2005GL024233>.
- Künsch, H. R., 1989: The jackknife and the bootstrap for general stationary observations. *Ann. Stat.*, **17**, 1217–1241, <https://doi.org/10.1214/aos/1176347265>.
- Latif, M., M. Collins, H. Pohlmann, and N. Keenlyside, 2006: A review of predictability studies of Atlantic sector climate on decadal time scales. *J. Climate*, **19**, 5971–5987, <https://doi.org/10.1175/JCLI3945.1>.
- Lee, T., and J. Marotzke, 1998: Seasonal cycles of meridional overturning and heat transport of the Indian Ocean. *J. Phys. Oceanogr.*, **28**, 923–943, [https://doi.org/10.1175/1520-0485\(1998\)028<0923:SCOMOA>2.0.CO;2](https://doi.org/10.1175/1520-0485(1998)028<0923:SCOMOA>2.0.CO;2).
- Leroux, S., T. Penduff, L. Bessières, J.-M. Molines, J.-M. Brankart, G. Sérazin, B. Barnier, and L. Terray, 2018: Intrinsic and atmospherically forced variability of the AMOC: Insights from a large-ensemble ocean hindcast. *J. Climate*, **31**, 1183–1203, <https://doi.org/10.1175/JCLI-D-17-0168.1>.
- Levitus, S., M. Conkright, T. P. Boyer, T. O'Brian, J. Antonov, C. Stephens, L. S. D. Johnson, and R. Gelfeld, 1998: World Ocean Database 1998. NOAA Atlas NESDIS Tech. Rep. 18, 346 pp.
- Lorenz, E. N., 1963: Deterministic nonperiodic flow. *J. Atmos. Sci.*, **20**, 130–141, [https://doi.org/10.1175/1520-0469\(1963\)020%3C0130:DNF%3E2.0.CO;2](https://doi.org/10.1175/1520-0469(1963)020%3C0130:DNF%3E2.0.CO;2).
- , 1982: Atmospheric predictability experiments with a large numerical model. *Tellus*, **34**, 505–513, <https://doi.org/10.3402/tellusa.v34i6.10836>.
- Lozier, M. S., and Coauthors, 2019: A sea change in our view of overturning in the subpolar North Atlantic. *Science*, **363**, 516–521, <https://doi.org/10.1126/science.aau6592>.
- Madec, G., and NEMO Team, 2016: NEMO ocean engine. Note du Pôle de modélisation de l'Institut Pierre-Simon Laplace 27, 386 pp., https://www.nemo-ocean.eu/wp-content/uploads/NEMO_book.pdf.
- Marzocchi, A., J. J.-M. Hirschi, N. P. Holliday, S. A. Cunningham, A. T. Blaker, and A. C. Coward, 2015: North Atlantic subpolar circulation in an eddy-resolving global ocean model. *J. Mar. Syst.*, **142**, 126–143, <https://doi.org/10.1016/j.jmarsys.2014.10.007>.
- McCarthy, G., and Coauthors, 2012: Observed interannual variability of the Atlantic meridional overturning circulation at 26.5°N. *Geophys. Res. Lett.*, **39**, L19609, <https://doi.org/10.1029/2012GL052933>.
- , I. D. Haigh, J. J.-M. Hirschi, J. P. Grist, and D. A. Smeed, 2015: Ocean impact on decadal Atlantic climate variability revealed by sea-level observations. *Nature*, **521**, 508–510, <https://doi.org/10.1038/nature14491>.
- Meinen, C. S., M. O. Baringer, and R. F. Garcia, 2010: Florida Current transport variability: An analysis of annual and longer period signals. *Deep-Sea Res. I*, **57**, 835–846, <https://doi.org/10.1016/j.dsr.2010.04.001>.
- Moat, B. I., and Coauthors, 2016: Major variations in subtropical North Atlantic heat transport at short (5 day) timescales and their causes. *J. Geophys. Res. Oceans*, **121**, 3237–3249, <https://doi.org/10.1002/2016JC011660>.
- NOAA, 2006: 2-minute Gridded Global Relief Data (ETOPO2) v2. NOAA National Centers for Environmental Information, accessed 8 April 2022, <https://doi.org/10.7289/V5J1012Q>.
- Rayner, D., and Coauthors, 2011: Monitoring the Atlantic meridional overturning circulation. *Deep-Sea Res. II*, **58**, 1744–1753, <https://doi.org/10.1016/j.dsr2.2010.10.056>.
- Rhines, P. B., 1977: The dynamics of unsteady currents. *Marine Modeling*, E. D. Goldberg, Ed., *The Sea—Ideas and Observations on Progress in the Study of the Seas*, Vol. 6, Wiley, 189–318.
- Roberts, C. D., and Coauthors, 2013: Atmosphere drives recent interannual variability of the Atlantic meridional overturning circulation at 26.58°N. *Geophys. Res. Lett.*, **40**, 5164–5170, <https://doi.org/10.1002/grl.50930>.
- Salmon, R. B., 1980: Baroclinic instability and geostrophic turbulence. *Geophys. Astrophys. Fluid Dyn.*, **15**, 167–211, <https://doi.org/10.1080/03091928008241178>.
- Sévellec, F., A. C. Naveira Garabato, and T. Huck, 2021: Damping of climate-scale oceanic variability by mesoscale eddy turbulence. *J. Phys. Oceanogr.*, **51**, 491–503, <https://doi.org/10.1175/JPO-D-20-0141.1>.
- Sime, L. C., D. P. Stevens, K. J. Heywood, and K. I. Oliver, 2006: A decomposition of the Atlantic meridional overturning. *J. Phys. Oceanogr.*, **36**, 2253–2270, <https://doi.org/10.1175/JPO2974.1>.
- Smeed, D. A., and Coauthors, 2018: The North Atlantic Ocean is in a state of reduced overturning. *Geophys. Res. Lett.*, **45**, 1527–1533, <https://doi.org/10.1002/2017GL076350>.

- Sonnevald, M., J. J.-M. Hirschi, and R. Marsh, 2013: Oceanic dominance of interannual subtropical North Atlantic heat content variability. *Ocean Sci. Discuss.*, **10**, 27–53, <https://doi.org/10.5194/osd-10-27-2013>.
- Srokosz, M. A., and H. L. Bryden, 2015: Observing the Atlantic meridional overturning circulation yields a decade of inevitable surprises. *Science*, **348**, 1255575, <https://doi.org/10.1126/science.1255575>.
- Steele, M., R. Morley, and W. Ermold, 2001: PHC: A global ocean hydrography with a high quality Arctic Ocean. *J. Climate*, **14**, 2079–2087, [https://doi.org/10.1175/1520-0442\(2001\)014<2079:PAGOHW>2.0.CO;2](https://doi.org/10.1175/1520-0442(2001)014<2079:PAGOHW>2.0.CO;2).
- Thomas, M. D., and X. Zhai, 2013: Eddy-induced variability of the meridional overturning circulation in a model of the North Atlantic. *Geophys. Res. Lett.*, **40**, 2742–2747, <https://doi.org/10.1002/grl.50532>.
- Timmermann, A., H. Goosse, G. Madec, T. Fichefet, C. Ethe, and V. Dulire, 2005: On the representation of high latitude processes in the ORCA-LIM global coupled sea-ice ocean model. *Ocean Modell.*, **8**, 175–201, <https://doi.org/10.1016/j.oceanmod.2003.12.009>.
- Wunsch, C., 2008: Mass and volume transport variability in an eddy-filled ocean. *Nat. Geosci.*, **1**, 165–168, <https://doi.org/10.1038/ngeo126>.